Simplified Modeling of Active Magnetic Regenerators

by

Thomas Burdyny
BEng., University of Victoria, 2010

A Thesis Submitted in Partial Fulfillment of the Requirements for the Degree of

MASTER OF APPLIED SCIENCE

in the

Department of Mechanical Engineering

© Thomas Burdyny, 2012
University of Victoria

All rights reserved. This thesis may not be reproduced in whole or in part, by photocopy or other means, without the permission of the author.

Simplified Modeling of Active Magnetic Regenerators

by

Thomas Burdyny
BEng., University of Victoria, 2010

Supervisory Committee

Dr. Andrew Rowe (Department of Mechanical Engineering)
Supervisor

Dr. Peter Oshkai (Department of Mechanical Engineering)
Departmental Member

Supervisory Committee

Dr. Andrew Rowe (Department of Mechanical Engineering)
Supervisor

Dr. Peter Oshkai (Department of Mechanical Engineering)
Departmental Member

Abstract

Active magnetic regenerator (AMR) refrigeration is an alternative technology to conventional vapor-compression refrigerators that has the potential to operate at higher efficiencies. Based on the magnetocaloric effect, this technology uses the magnetization and demagnetization of environmentally neutral solid refrigerants to produce a cooling effect. To become competitive however, a large amount of research into the optimal device configurations, operating parameters and refrigerants is still needed. To aid in this research, a simplified model for predicting the general trends of AMR devices at a low computational cost is developed. The derivation and implementation of the model for an arbitrary AMR is presented. Simulations from the model are compared to experimental results from two different devices and show good agreement across a wide range of operating parameters. The simplified model is also used to study the impacts of Curie temperature spacing, material weighting and devices on the performance of multilayered regenerators. Future applications of the simplified AMR model include costing and optimization programs where the low computational demand of the model can be fully exploited.

Table of Contents

List of Figures

List of Tables

Nomenclature

Acronyms

AMR(R)	Active Magnetic Regenerator (Refrigerator)
MCE	Magnetocaloric Effect (adiabatic temperature change)
COP	Coefficient of Performance
AMRTA	Active Magnetic Regenerator Test Apparatus
PMMR1	Permanent Magnet Magnetic Refrigerator

Symbols

a, b, c, d	Discrete points in a cycle	-
A	Surface area	m^2
B	Magnetic Field	T
Bi	Biot number	-
c	Specific heat	$JkgK^{-1}$
d	Diameter	m
DF	Degradation factor	-
Fo	Fourier number	-
h	Convection coefficient, enthalpy	$Wm^{-2}K^{-1}$, $kJkg^{-1}$
H	Enthalpy rate	W
k	Thermal conductivity	$Wm^{-1}K^{-1}$
L	Length	m
m	Mass	kg
n	MCE scaling exponent	-
Pr	Prandtl number	-
p	Pressure	Nm^{-2}
Q	Heat transfer rate	W
R	Thermal mass ratio	-
Re	Reynold's number	-
s	Entropy	$kJkg^{-1}K^{-1}$
t	Non-dimensional time coordinate	-

T	Temperature	K
U	Utilization	-
W	Power	W
x	Non-dimensional spatial coordinate	-

Greek

α	Thermal diffusivity	m^2s^{-1}
β	Balance	-
ε	Porosity	-
Γ	Geometric form factor	-
κ	Non-dimensional conductance	-
ρ	Density	kgm^{-3}
σ	Symmetry	-
τ	Period	s
Φ	Utilization	-

Subscripts

C	Cold or cooling capacity	-
c	Cycle	-
eff	Effective	-
f	Fluid	-
H	Hot or high-field	-
h	Hydraulic	-
m	Magnetic	-
p	Constant pressure, parasitic	-
s	Solid	-
$'$	Per unit length	-

Acknowledgements

Two years ago, when I began my master's program, I was unsure of the type of research I wanted to pursue. While striving to think of something unique to study in the broad fields of thermodynamics and energy I wandered, with gentle nudges from my supervisor, into the world of magnetic refrigeration. Two years later I could not be more pleased with the result and consider myself lucky to have been given the opportunities that I have.

First and foremost I'd like to thank my supervisor Andrew Rowe. During several phases of my research, when progress was either slow or stalled, he always managed to find the perfect balance of assistance and guidance that allowed me to better understand and appreciate not only my project but the research process in general. When I did ask for assistance, he always found the time to help and I apologize for the multiple occasions I probably made him late for other obligations by doing so.

Also invaluable to both my research and sanity was the Cryofuels group. Armando Tura, Danny Arnold, Oliver Campbell, Alex Ruebsaat-Trott and Sandro Schopfer have shared their individual knowledge over the last couple years and merely being present at our (early) morning meetings with them has had the innate ability to motivate me to keep pushing onward when progress was slow. More important, however, are the innumerable fun times we have had outside of the university ranging from late nights on the deck at Armando's house to travel abroad.

I'd also like to thank my family and friends for their unwavering support amidst my ups and downs and occasional periods of invisibility. Finally I'd like to acknowledge financial support from the Natural Sciences and Engineering Research Council of Canada and funding provided by the H2Can Strategic Network which was essential in bringing this research to fruition.

Chapter 1 – Introduction

1.1 Overview

As the world becomes more technologically advanced and the overall worldwide standards of living improve, energy consumption is increasing at a large rate. Coupled with concerns over the rising levels of CO_2 in the atmosphere and its projected impact on the planet's climate, the production of clean energy has become an important research focus in academia and industry. In parallel to energy production, it is also important to improve the efficiency and reduce the environmental impact of service technologies which convert energy carriers into usable heat and work. One technology which has a large impact on both the production and consumption of energy carriers is refrigeration.

Refrigeration processes are currently used worldwide in a variety of applications including domestic cooling, food preservation and gas liquefaction. With the slow but steady progression towards using hydrogen in fuel cell vehicles, the production of liquid hydrogen via refrigeration is also likely to increase in the future. Conventional refrigeration uses the compression and expansion of a vapour to produce either a heating or cooling effect. This technology has been proven robust and has fully penetrated into both the industrial and domestic markets, making it mature and relatively inexpensive to build. For applications near room temperature, however, the most efficient operating fluids are chlorofluorocarbons (CFC's) which are known to deplete the ozone layer. Additionally, the continuous compression/expansion processes are susceptible to large irreversibilities which lower the device operating efficiency. These losses are particularly problematic for liquid hydrogen production where increasing costs hinders hydrogen's viability to be used as an energy carrier. An alternative to conventional vapor-compression refrigeration technology is magnetic refrigeration.

In magnetic refrigeration the cooling effect is produced through the magnetization and demagnetization of an environmentally neutral solid refrigerant instead of conventional two-phase refrigerants. Furthermore, the magnetic cycle does not require compressors or throttles allowing for the compression and expansion irreversibilities seen in conventional refrigeration to be avoided. This results in a theoretical increase in device operating efficiency over conventional systems [1]. Magnetic refrigeration however, despite being

used for almost a century in a wide variety of laboratory applications, is relatively immature and has yet to be produced for commercial purposes.

1.2 MAGNETIC REFRIGERATION

1.2.1 THE MAGNETOCALORIC EFFECT

Magnetic refrigeration is based upon a phenomenon known as the magnetocaloric effect (MCE). Due to this phenomenon a substance introduced into a magnetic field, B, will increase in temperature by a predictable and repeatable amount, ΔT_{ad}. The increase in temperature depends on the material, absolute temperature and magnetic field strength and for some materials is significant enough to form the basis of a thermal cycle. This effect can be almost fully reversible or exhibit hysteresis depending on the material. In the reversible case removing the magnetic field will cause the material to revert back to its original temperature.

The thermodynamics of the MCE can be explained by observing the entropy of a material during magnetization. The total entropy of a material is the sum of the magnetic, S_m, lattice S_l, and electric, S_e, entropies. Once introduced to a magnetic field the magnetic moments within a material align causing a decrease in the magnetic entropy. Since magnetizing a soft magnetic material adiabatically is an isentropic process however, the total material entropy remains constant. The reduction in the magnetic entropy then corresponds to an increase in the material's lattice entropy. Due to the influence of lattice entropy on temperature this results in an adiabatic increase in temperature, ΔT_{ad}. This process is shown in Figure 1-1 for Gd undergoing a field change from 0 T to 2 T. Removal of the magnetic field results in the opposite isentropic process.

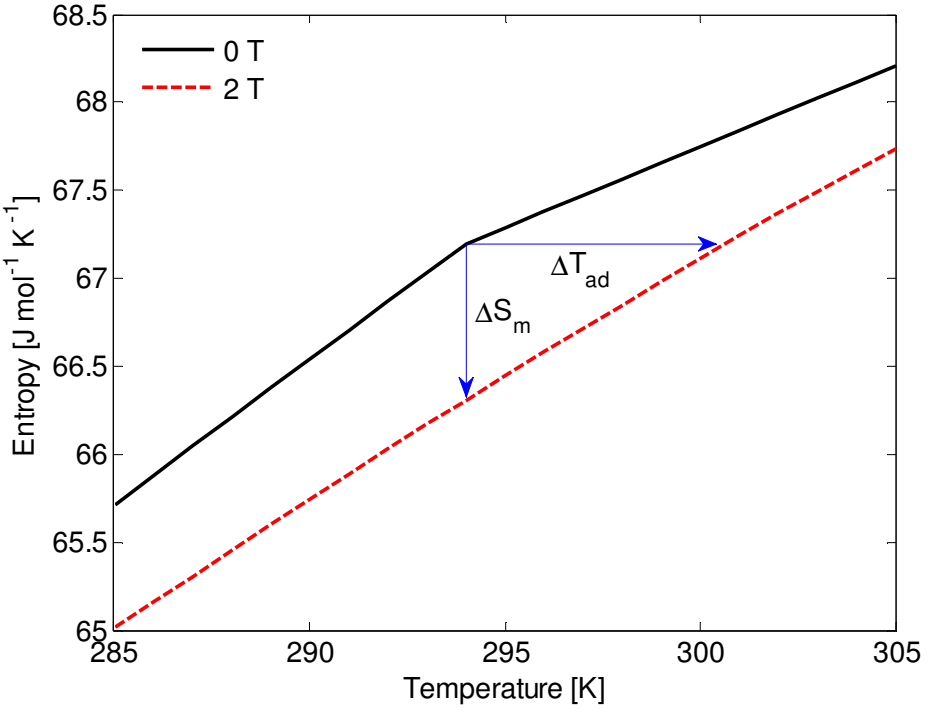

Figure 1-1: Entropy of Gd at 0 T and 2 T. The changes in the magnetic entropy and MCE (ΔT_{ad}) during magnetization are shown at the Curie temperature of Gd, 294 K.

The magnitude of the MCE is material, temperature and field dependent. Materials can be characterized by their maximum MCE per Tesla of magnetization and the temperature at which that maximum MCE occurs, known as the Curie temperature, T_{Curie}. At this temperature second-order materials undergo a phase transition from ferromagnetic to paramagnetic, resulting in a reduced capacity for the material to maintain its magnetization. The rare-earth metal Gadolinium, Gd, has a Curie point at approximately 294 K while its alloys $Gd_{0.85}Er_{0.15}$ (GdEr) and $Gd_{0.74}Er_{0.26}$ (GdTb) have Curie points near 269 K and 278 K, respectively. The Curie point and the MCE's dependence on field strength and temperature are demonstrated in Figure 1-2 for Gd. As one would expect, increasing the magnetic field applied to the material produces a larger MCE due to a larger change in the magnetic entropy. The MCE also diminishes quite quickly away from the Curie point meaning that the material's effectiveness decreases when operating over a wider range of temperatures.

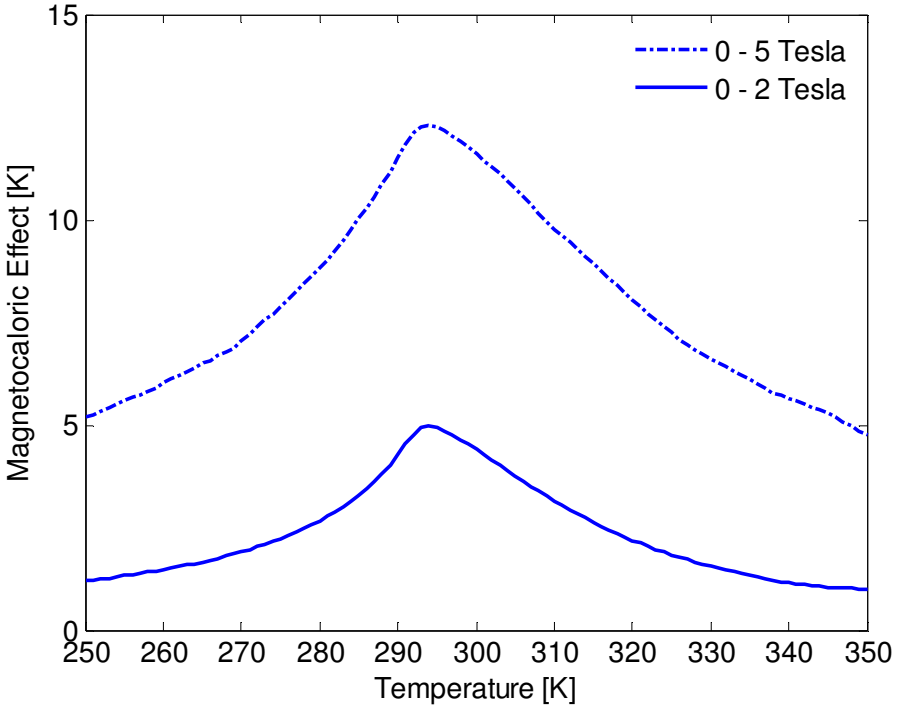

Figure 1-2: MCE as a function of temperature and field for Gd.

Materials used in magnetic refrigeration applications are typically classified as either first-order or second-order materials based upon the type of phase transitions that occur in the material. Second-order materials such as Gd are characterized by a gradual decrease in the MCE from the Curie point which gives moderate temperature change over a wider operating region. First-order materials, on the other hand, can have a much larger peak MCE than second-order materials but the magnitude of the temperature change decreases rapidly as the material operates further away from the Curie point.

1.2.2 HISTORY

Although first noticed in 1881 by Warburg [2], the magnetocaloric was not explained until 1918 by Weiss and Picard [3]. Magnetic cooling was then applied in 1933 [4],[5] in the form of one-shot cooling methods with the purpose of producing sub-Kelvin temperatures. This process involved magnetizing an entire mass of material, reducing the temperature back to its original value and then demagnetizing the system to achieve a low temperature thermal mass. This method is still used for applications between 0 K and 4 K but is not practical for applications requiring continuous cooling.

A lack of functional magnetocaloric materials above 20 K then prevented the technology from advancing until the 1970's when Brown discovered that ferromagnetic materials produced a sizeable change in temperature when magnetized near their Curie points [6]. This then resulted in experiments near room temperature using gadolinium but performance was limited by the use of passive regenerators and heat exchangers in the refrigeration cycle. The concept of an Active Magnetic Regenerator (AMR) was then suggested by Barclay and Steyert in 1982 [7] which greatly improved performance by using the refrigerant itself as an active regenerator in the refrigeration cycle. This is the current cycle used in today's magnetic refrigerators.

1.2.3 The Active Magnetic Regenerator

In the first room temperature applications passive regenerators were used to reject and absorb heat from a magnetic refrigerant after it had been magnetized and demagnetized. A working fluid acted as an intermediate means of transferring the heat between the two. In this case, the entire refrigerant thermal mass underwent a single adiabatic temperature change. With this approach however, the maximum attainable temperature difference between the thermal reservoirs is then limited by the adiabatic temperature change which, for most materials, is only around 2 K/T of applied field. Producing spans large enough for practical applications would then require very high field strengths which are expensive to produce. The passive regeneration process could also produce only limited amounts of cooling power due to the large cycle times needed for heat transfer. For these reasons the concept of the active magnetic regenerator was developed.

In an AMR device the refrigerant itself acts as the regenerator, making it an active part of the refrigeration cycle. This is possible due to the high heat capacities of common magnetocaloric materials near their Curie temperatures. It is also highly effective due to the high heat transfer area already needed between the working fluid and solid refrigerant in the refrigeration cycle. Once the refrigerant is used as a regenerator a much larger steady state temperature difference is possible across the material bed. This is because the cyclical heat transfer within a regenerator, due to the cold and hot blows from the thermal reservoirs, causes a temperature gradient to be developed between the two ends. Material along the regenerator then undergoes its own local adiabatic temperature change

depending upon the temperature of the bed at that point. The cumulative effect of these individual cycles allows for large temperature spans at a low magnetic field compared to the single magnetic cycle in the passive devices. The next section describes in more detail how the active magnetic regenerator is used to create a refrigeration cycle.

1.2.4 AMR Refrigeration Cycle

The magnetocaloric effect can be used to increase and decrease the temperature of a material through magnetization and demagnetization, respectively. By using a heat transfer fluid to intermittently exchange heat with the solid refrigerant, a refrigeration cycle can be formed whose process is similar in theory to conventional vapour-compression systems. This comparison between a conventional refrigeration cycle and the cycle which occurs locally within the refrigerant of an AMR cycle can be seen in Figure 1-3. Although this figure only describes the local steps within magnetic refrigeration cycles, the effect of these individual cycles along the regenerator bed is responsible for the developed temperature span.

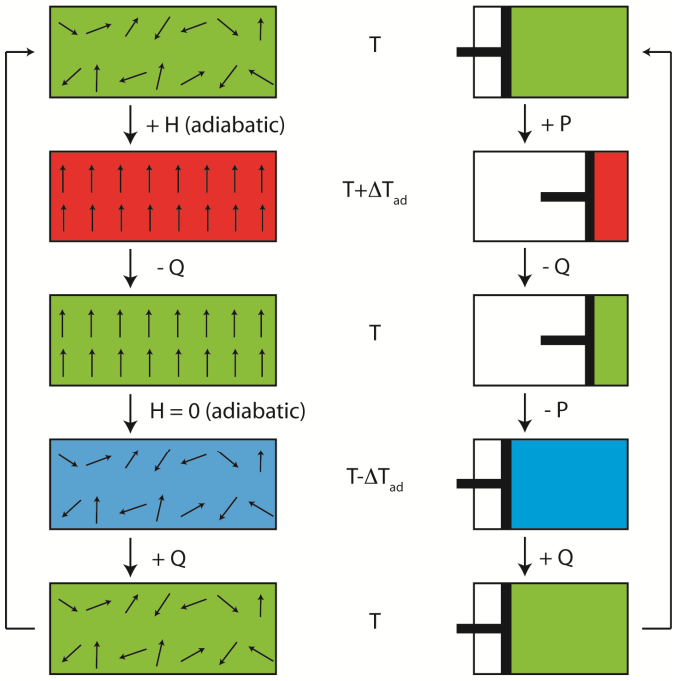

Figure 1-3: Comparison of the individual steps in a local magnetic refrigeration cycle and a vapour-compression refrigeration cycle. *H* represents a magnetic field.

The above refrigeration process can be approximated by four individual steps. These are described below and represented on a *T-s* diagram in Figure 1-4. Points *a'-b-c'-d*

represent the state points of the solid refrigerant while *a-b-c-d* are the fluid temperatures at each of the four states. This difference is due to the almost instantaneous temperature change to *a'* and *c'* for the refrigerant while thermal equilibrium between the fluid and the solid requires more time and is reached at *a* and *c* respectively. Based upon the convention used in developing the simplified model in this thesis, the magnetic cycle starts at state *b* to comply with the presented theory. In an actual device, the following processes also partially overlap due to the sinusoidal nature of the magnetic field and the fluid being pumped through the system:

b – c': Adiabatic magnetization of the regenerator causing an isentropic temperature increase from *b* to *c'*.

c' – d: Displacement of the heat transfer fluid through the regenerator bed from the cold side to the hot side reduces the bed temperature.

d – a': Adiabatic demagnetization of the regenerator causing an isentropic temperature decrease from *d* to *a'*.

a' – b: Displacement of the heat transfer fluid through the regenerator bed from the hot to side to the cold side increases the bed temperature.

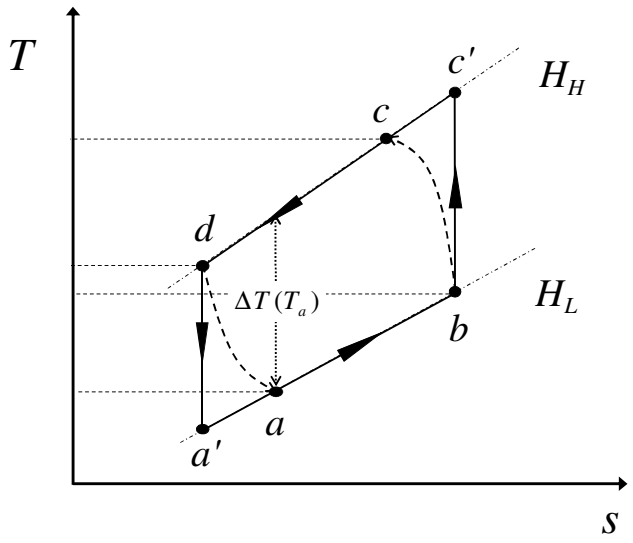

Figure 1-4: T-s diagram of the magnetic cycle occurring locally within an AMR system, H_H and H_L are high and low fields, respectively. *a'* and *c'* represent the temperature of the solid refrigerant after a field change while *a* and *c* represent the equilibrium temperature of the solid and fluid [8].

From this local magnetic cycle an AMR refrigeration cycle can be created. This requires choosing the number of regenerators, geometry of the regenerator, type of working fluid and the relative movement of the magnet and regenerator. Coupled with the large amount of usable materials and plethora of operating parameters, an AMR refrigerator can be designed in many different ways. Figure 1-5 shows a representative AMR refrigeration cycle that uses a reciprocating magnet which alternates between two identical regenerators. The cold and hot fluid blows are provided through the movement of a piston displacer while heat is exchanged with the environment through cold and hot heat exchangers. In experimental devices the hot heat exchanger is controlled by chillers in order to fix the hot end temperature, T_H, while the cooling capacity, Q_C, is provided by an electric heater so that it can be controlled in experiments. Both of these allow the device and materials to be tested and compared at controlled operating conditions. The cold end temperature, T_C, is then allowed to vary. As shown in the figure, the temperature span is defined as the difference between T_H and T_C which are calculated as the steady state fluid temperatures at the ends of the regenerator.

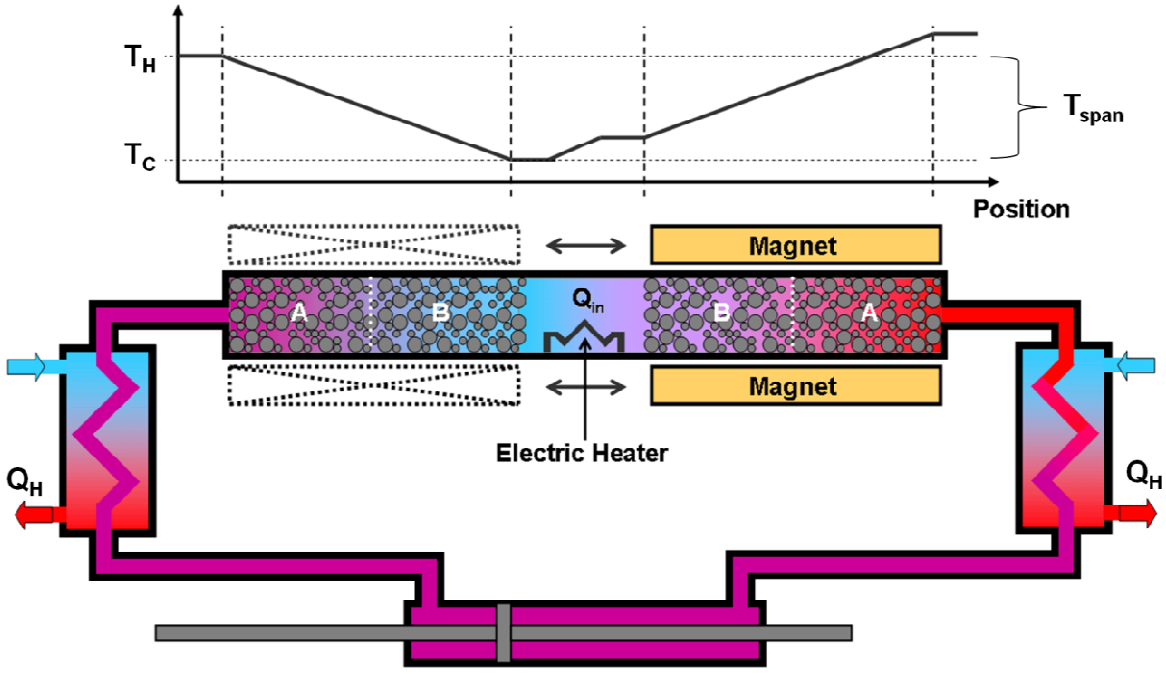

Figure 1-5: Simplified representation of an AMR apparatus showing the simplified temperature profile across the regenerator [9]. A displacer and heat exchangers are required in the cycle.

In experimental devices it is common to have two regenerators in opposite parts of their respective magnetic cycles so that the magnetic field is utilized during the whole

cycle. Having the regenerators on opposite sides of the cycle also allows for the device to provide more continuous cooling by having essentially two cold blows (one for each regenerator) per cycle. Figure 1-5 also shows the material bed containing two different materials, A and B. This is done as using a multilayer regenerator can provide higher temperature spans than a bed with only one material.

1.2.5 MULTILAYER REGENERATORS

Layering more than one type of material together in a regenerator can improve AMR performance by increasing the average MCE along the bed. As shown in Figure 1-2, the peak temperature change for a magnetocaloric material occurs at the Curie temperature; magnetizing a material either above or below this temperature results in a reduced MCE. In the steady state operation of an AMR a temperature gradient exists from T_H to T_C (Figure 1-5). This means that in a single material regenerator only a small section will be operating at the Curie temperature, where the material's peak MCE exists. The remainder of the regenerator will undergo a smaller temperature change and hence a smaller local magnetic cycle. Adding a secondary material that has a different Curie temperature to the bed would then allow for the average MCE across the bed to be increased by now providing a secondary temperature where a peak MCE occurs.

A rudimentary analysis of this effect is shown in Figure 1-6 where the Gd and GdEr MCE curves for a field change are plotted over a selected range of temperatures. Also plotted is the average MCE over the operating range of single-layer (Gd) and two layer (Gd-GdEr) regenerators. This range is chosen as the temperature spans based on experimental results by Tura [10]. In experiments, the single-layer regenerator of Gd produced a temperature span of 34.8 K from T_H = 304.4 K to T_C = 269.6 K for an average MCE of 2.9 K while the two layer regenerator had a temperature span of 42 K and an average MCE of 3.4 K. Results by Tura showed that in the two layer case the temperature spans of the individual layers were almost equal at the given T_H value. This increase in the average MCE ultimately resulted in a higher temperature span for the two layer regenerator over the single-layer bed. As can be expected, layering additional materials in the regenerator could increase the average MCE across the bed even more.

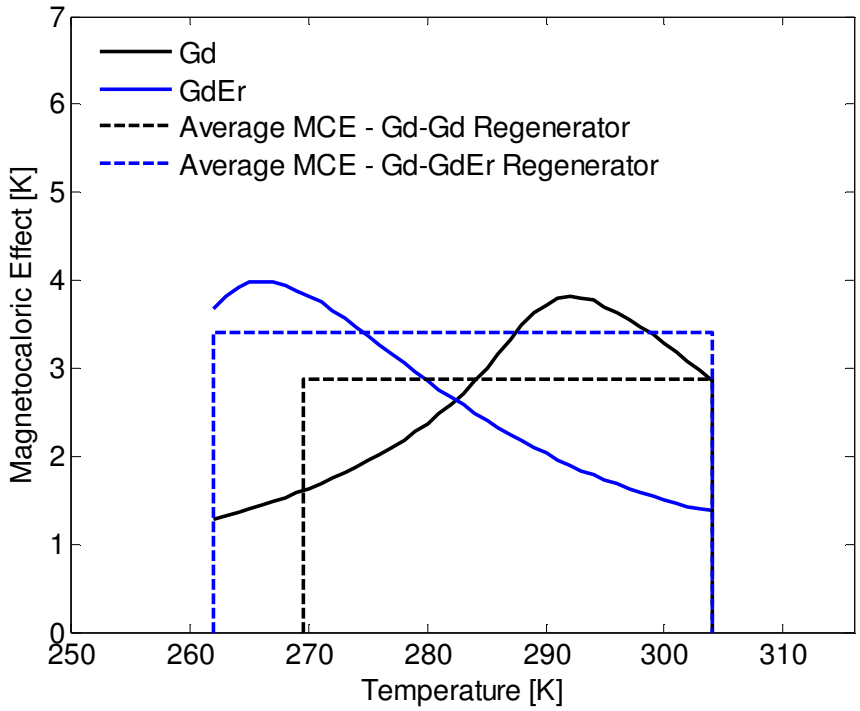

Figure 1-6: Comparison of the average MCE across a material bed for experimental results using a Gd-Gd and a Gd-GdEr regenerator where T_H = 304.4 K and Q_C = 0 W. The temperature span for Gd-Gd is 34.8 K and for Gd-GdEr is 42 K [10].

Although the basic premise of layering regenerators is understood, a great deal of research is required to determine the intricacies of this concept. This includes the optimal spacing of the Curie temperatures between materials and whether the proportions of each material should be different. This is further complicated by the effects that devices themselves have on the ability of layering to increase performance. Researching layered regenerators then requires either a large amount of experimental results or a numerical model capable of replicating the performance of an AMR device. A number of these AMR models have been created and are discussed in the following section.

1.2.6 AMR MODELING

The physics occurring within an AMR device are quite complex. Analyzing the thermal cycle of the solid and fluid within the regenerator requires taking into account two-phase heat transfer, fluid dynamics, thermodynamics and magnetic fields. Additionally, physical design constraints and irreversible losses due to demagnetization

effects, hysteresis and flow channeling all depend highly on the physical setup of the device being simulated.

One means of predicting the performance of an AMR is a higher-order model that takes solid/fluid interactions into account on a nodal basis. This is particularly useful for fundamentally understanding the intricacies of what occurs inside an AMR. A number of these models have been produced in recent years with a broad range of applications and resolutions [11]-[17]. A recent description of published models has been reported by Nielsen et al [18]. These higher-order models vary amongst themselves in complexity ranging from 1D to 2D and time dependent or time independent. Some of the models also use temperature varying fluid properties and account for axial conduction and viscous dissipation within the regenerator. Detailed modeling of this approach requires small time steps to replicate the constantly varying magnetic field and fluid velocity which increases the time to obtain a solution. Additionally, due to the complexity of the system these models are usually forced to analyze the regenerators only instead of the entire refrigeration cycle. This reduces the number of models that have been validated for a large variety of experimental results. If the higher-order model is used in replicating an actual device, external losses due to environmental heat leaks or eddy currents are then usually added to the model after a solution has been found; this approach then detracts from some of the attention to detail taken beforehand. All of these factors contribute to a large computational drain in order to solve a single set of operating conditions. This reduces the capacity of a thorough model to be used in guiding experiments or determining the optimal operating conditions of a system. Simpler AMR models have therefore been created with the intention of providing quick solutions to guide in the overall design of a device.

Simplified AMR models are willing to sacrifice a level of detail in order to reduce computational demand. The main priorities are replicating the general trends and sensitivities of a device in a quick manner. This is usually done through a periodic steady state solution where the temperature span of the regenerator is not developed over time numerically but solved in the form of a differential equation. A number of these models have been created with purposes ranging from entropy minimization to cryogenic applications [19]-[21]. Due to the simplicity of these models the overall AMR device can

be simulated which makes comparisons to experimental results easier. This then allows a large operating space to be compared against experiments and problematic areas to be identified. Correlations can also be developed in higher-order models and then transferred to the simpler models.

In this thesis a model based on work by Rowe [8],[22] is created to aid the general AMR design process. This model uses a steady state approach in solving the regenerator energy balance and relies on correlations and other modeling results to replicate experimental results. Its intent is to focus more on issues such as component sizing, cost analysis and overall system optimization. Previously, the model was used to determine the performance of AMR refrigerators using idealized material properties [22]. This thesis uses the same thermodynamic formulation but with real material properties and regenerator characteristics. The objectives of this simplified model are described next.

1.3 OBJECTIVES

An AMR device uses magnetically induced temperature changes in solid materials to vary the temperature of a heat transfer fluid. With additional research, this technology has the potential to operate at a higher efficiency than conventional refrigeration processes, thus reducing the environmental impact of this service technology. The design of devices using AMR cycles is complicated however by the time varying heat transfer interactions between the fluid and solid and the many geometric and operational parameters. Performance is also strongly impacted by the field and temperature dependence of magnetic material properties. Since testing the entire operating space of an AMR device is too expensive and time consuming using experiments alone, it is then imperative for models to be created that can provide design insights in parallel.

The objective of this work is to create a simplified AMR model that is capable of replicating and predicting the general trends and sensitivities of an arbitrary AMR device. This means the underlying theory must be adaptable and not only applicable to a single device. To test this objective the model is compared against results for two very different AMR devices that vary by working fluid, magnetic field profile and losses. It must also be quick relative to other existing models such that it can be used for predictive results and run in optimization programs. An additional objective is for the model to fully

function without significant knowledge of heat transfer, thermodynamics or fluid dynamics. This requires it to be robust in operation over a large range operating conditions that may or may not have been explicitly tested. Finally, it is desired that adding devices or materials to the model's database can be done with ease such that the model can be easily updated as technology progresses.

The following chapter introduces the equations and assumptions governing the simplified model's operation. This is followed by a generalized description of losses in AMR devices. Chapter 3 describes the implementation of the theory into a modeling environment including how experimental inputs are represented within the model. Validation is performed against two experimental devices in Chapter 4. Chapter 5 focuses on using the model in researching the effects that layered regenerators have on AMR performance relative to single-layer beds. Chapter 6 subsequently contains a more critical analysis on both the validation and predictive results. Lastly, based upon the presented results, conclusions are drawn as to the simplified model's ability to achieve the defined objectives.

Chapter 2 – Model Development

This chapter introduces the governing equations for the model in addition to the underlying assumptions used in their derivation. Losses within an AMR device are then expressed in a form that can be used within a simplified AMR model.

2.1 ASSUMPTIONS

Two sets of governing equations are needed to determine the steady state temperature profile and cooling capacity of the AMR device in the simplified model. The assumptions used in development of these equations are listed below and justified afterward:

- One spatial dimension along the length of the regenerator is sufficient to model the energy interactions.
- Large heat transfer exists between the magnetic material and the working fluid such that $T_f \cong T_s = T(x,t)$.
- The effects of diffusion and viscous dissipation in the governing equation are negligible relative to the other terms.

The first two approximations allow for the fluid and solid heat transfer equations to be combined into one and are essential for a simplified model. Assuming one spatial dimension is done in the majority of existing AMR models with the loss of accuracy compared to a two dimensional model considered minimal. Assuming perfect heat transfer between the solid and fluid removes the impact of convection in the governing equations. Convection, however, is very important to the effectiveness of the regenerator and the resulting temperature span. For this reason the heat leak from convection is converted into an equivalent thermal conductivity and is still capable of impacting the AMR's performance. This is further discussed in Section 2.3.2. The final assumption is another common compromise made in both simple and complex AMR models. It should be noted that diffusion and viscous dissipation are included in the periodic steady state energy balance equation and are only ignored in the heat transfer governing equation for simplicity.

Further assumptions are used in the development of the entire model but these will be discussed as they appear. The governing equations can now be presented.

2.2 GOVERNING EQUATIONS

The first governing equation, seen in Eqn (1), describes the local energy balance of an AMR device in space and time [8]. Rowe showed that this equation, when coupled with equations describing the thermal equilibriums between the fluid and solid after a field change, can be used to relate the fluid temperatures at state points in the magnetic cycle to one another (see Figure 1-4). Thus if the temperature at one of the states points is known, the other three can be found. The governing equations are also non-dimensionalized by the blow period in time, $\tilde{t} = \tau_B t$, and regenerator length in space, $\tilde{x} = Lx$.

$$\frac{\partial T}{\partial t} = -\frac{\Phi}{R}\frac{\partial T}{\partial x} + \frac{1}{R}\frac{\partial T_{ad}}{\partial t} \tag{1}$$

where

$$\Phi = \frac{\dot{m} c_p \tau_B}{m_s' c_B L} \tag{2}$$

$$R = 1 + \frac{m_f' c_p}{m_s' c_B} \tag{3}$$

$$\frac{\partial T_{ad}}{\partial t} = -\frac{T}{c_B}\left(\frac{\partial M}{\partial T}\right)_H \frac{\partial \mu_0 H}{\partial t} \tag{4}$$

Eqn (2) is the utilization; this represents the ratio of the heat capacity of the fluid during a blow compared to the regenerator's total heat capacity. The thermal mass ratio, R, is the ratio of entrained fluid's thermal mass as compared to the total thermal mass. The final term in Eqn (4) represents the change in magnetocaloric effect in time.

In order to determine the temperature at one of the state points across the regenerator, $T_a(x)$, an energy balance can be performed along its length. A schematic of the thermodynamic quantities in the regenerator is shown in Figure 2-1.

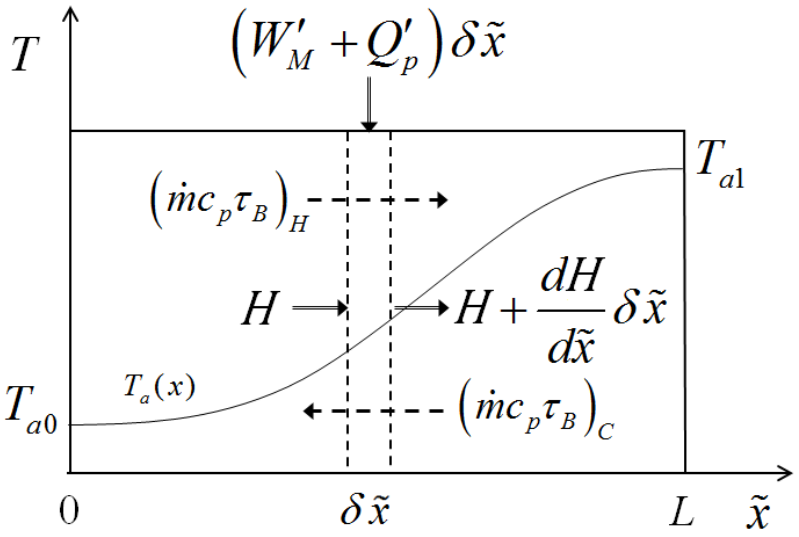

Figure 2-1: Representation of the thermodynamic terms occurring in an AMR regenerator in steady state operation [8].

In this figure the incremental increase in enthalpy rate, H, due to the magnetic work, W_M, and parasitic losses, Q_p, is shown. Also illustrated is the thermal mass of the cold and hot fluid blows denoted by the subscripts C and H, respectively. The below expressions derived by Rowe define the energy balance in the regenerator in steady state.

$$H = \frac{m_s' L c_s}{\tau_c}\Phi_{RH}\left[(1-\beta)\frac{h_a}{c_p} + \frac{\Delta T}{R_H} + \left(f_1 U_H - \frac{\kappa}{\Phi_{RH}}\right)\frac{dT}{dx}\right] \tag{5}$$

$$W_m{}' = \frac{m_s' c_s}{\tau_c}\frac{\Delta T}{T}c_{RH}\left[(R_H - 1)\left(1 - \frac{n}{n+1}\frac{1}{\sigma}\frac{d\Delta T}{dT}\right)\frac{\Delta T}{R_H} + (f_2 + (R_H - 1)f_3)U_H\frac{dT}{dx}\right] \tag{6}$$

$$W_m{}' + Q_p{}' = \frac{1}{L}\frac{dH}{dx} \tag{7}$$

Eqn (5) describes the net transfer of heat at any location in the AMR, Eqn (6) is the local rate of magnetic work, and Eqn (7) is the periodic steady-state energy balance. Parameters $f_1 - f_3$ are:

$$f_1 = \left(\frac{U_C}{U_H} - \frac{1}{2}\right)\left(1 + \frac{1}{R_H}\frac{d\Delta T}{dT}\right) - \frac{\beta}{2}\frac{U_C}{U_H} \tag{8}$$

$$f_2 = 1 + \left(\frac{1}{R_H} - \frac{n}{n+1}\frac{U_C}{U_H}\right)\frac{d\Delta T}{dT} \tag{9}$$

$$f_3 = \left[\frac{U_C}{U_H}\frac{1}{R_H} - \frac{n}{n+1}\frac{1}{\sigma}\left(\frac{U_C}{U_H} - 1\right)\left(1 + \frac{1}{R_H}\frac{d\Delta T}{dT}\right)\right]\frac{d\Delta T}{dT} \tag{10}$$

while the parameter β is defined as the balance between the fluid's thermal mass during the cold and hot blows and the symmetry, σ, is defined as the ratio of the refrigerant's specific heat at the low and high field strengths. These are important as the fluid and refrigerant properties vary by temperature and field.

$$\beta = \frac{\left(\dot{m}c_p\tau_B\right)_C}{\left(\dot{m}c_p\tau_B\right)_H} \tag{11}$$

$$\sigma = \frac{c_C}{c_H} = \frac{c_B(T, H_L)}{c_B(T + \Delta T, H_H)} \tag{12}$$

The governing equations are derived assuming a step-wise variation in field and fluid flow and the temperatures at different points in the cycle are determined in reference to point *a* – the local temperatures at the beginning of the cold blow. In the most general case, one can numerically solve Eqn (7) to determine the temperature distribution for specified boundary temperatures and then calculate work and heat transfer.

2.2.1 Second-Order Refrigerants Near Room Temperature

The experiments simulated using the model use second-order refrigerants in room temperature devices. This allows for some simplifications of the governing equations used in the model.

Because the thermal capacity of the heat transfer fluid depends on temperature and pressure, the possibility exists for the flow to be thermally imbalanced between the hot and cold blows. For common heat transfer fluids near room temperature however the variation in specific heat and density is small enough that the balance can be assumed to be equal, giving $\beta = 1$. It is also assumed that the magnetocaloric effect of second-order materials scales proportional to the field strength, therefore $n = 1$. For comparison to experimental results, only β and n are assumed.

With these assumptions Eqns (5) and (6) are inserted into Eqn (7) which produces the differential equation describing the temperature profile immediately before the fluid flow commences at low field.

$$a_2\frac{d^2T}{dx^2}+a_1\frac{dT}{dx}+a_0=\frac{\tau_c}{m_s' L c_s}Q_p$$

$$a_0=\ c_{RH}\left(\frac{R_H-1}{R_H}\right)\left(1-\frac{1}{2\sigma}\frac{d\Delta T}{dT}\right)\frac{\Delta T^2}{T} \tag{13}$$

$$a_1=\ \frac{\Phi_{RH}}{R_H}\left((f_2+(R_H-1)f_3)\frac{\Delta T}{T}-\frac{d\Delta T}{dT}-\frac{d(f_1U_H)}{dT}\right)$$

$$a_2=\ \kappa-f_1\Phi_{RH}U_H$$

where

$$\frac{d(f_1U_H)}{dT}=\left(\frac{dU_C}{dT}-\frac{1}{2}\frac{dU_H}{dT}\right)\left(1+\frac{1}{R_H}\frac{d\Delta T}{dT}\right)-\frac{\beta}{2}\frac{dU_C}{dT}+\left(U_C-\frac{U_H}{2}\right)\frac{1}{R_H}\frac{d^2\Delta T}{dT^2} \tag{14}$$

Solution of Eqn (13) requires two boundary conditions, T_{a0} and T_{a1}, which results in the temperature distribution of a single state point, $T_a(x)$, across the regenerator. Knowledge of the magnetic cycle allows for the other three state temperatures to be determined in reference to point *a* [8]. The average fluid temperature in Eqn (15) is subsequently assumed to be the average of the four states of the cycle.

$$\overline{T_f}=\frac{1}{4}(T_a+T_b+T_c+T_d) \tag{15}$$

The fluid temperatures at the ends of the regenerator, $T_f(x=0)$ and $T_f(x=L)$, are then comparable to the fluctuating temperature measurements taken during experiments. These are then identified as T_C and T_H, respectively, which define the temperature span of the regenerator, T_{Span}. With the temperature span and profile determined, the cooling capacity for the given operating parameters can be evaluated. This requires accounting for losses external to the regenerator due to eddy currents and ambient heat leaks. It is also important to quantify the unavoidable losses occurring within the regenerator itself.

2.3 AMR Loss Mechanisms

Loss mechanisms existing in an AMR refrigerator include parasitic losses within the regenerator and losses external to the regenerator. The general AMR device schematic in Figure 2-2 shows the thermodynamic exchanges occurring within a typical device.

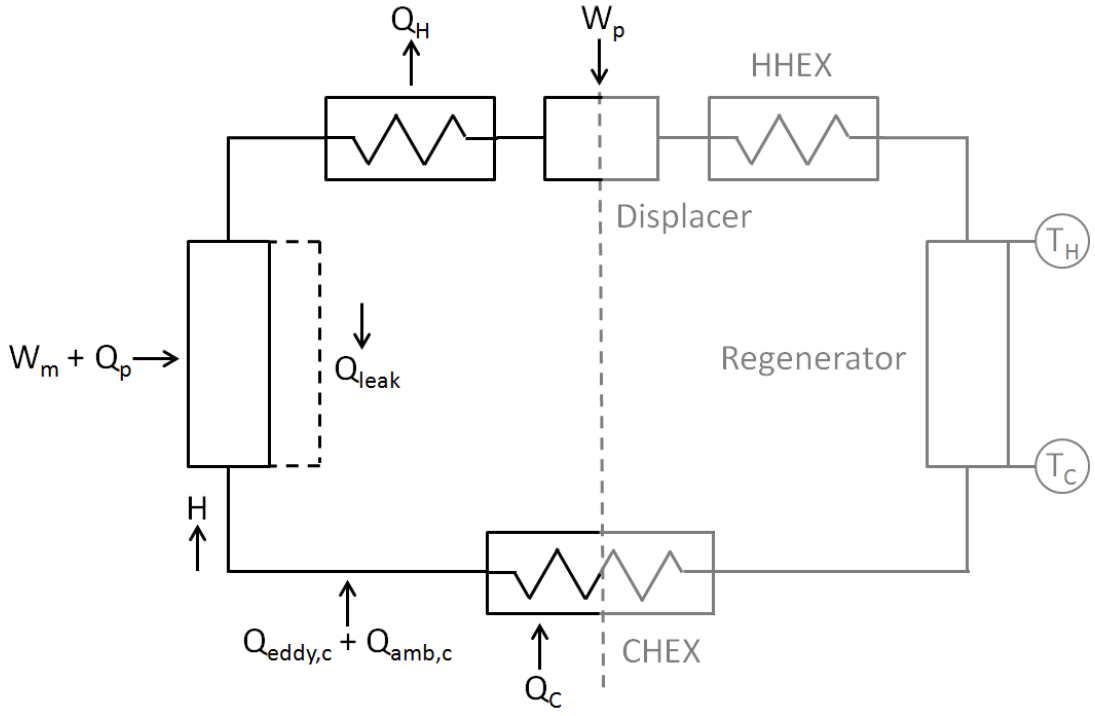

Figure 2-2: Schematic of the general components in an AMR device (right) and thermodynamic exchanges (left) within the system include work inputs, losses and enthalpy across the regenerator.

2.3.1 Parasitic Losses

The parasitic losses appearing in Eqns (7) and (13) are those occurring within the regenerator and across its boundaries. This includes eddy currents in the magnetic material, ambient heat leaks through the regenerator shell and viscous dissipation due to fluid pressure drop in the regenerator matrix. Therefore, the regenerator losses per unit length are

$$Q_p' = Q_{eddy}' + Q_{amb}' + Q_{viscous}' \tag{16}$$

These losses are specific to the device design and operating conditions. The viscous dissipation term is calculated using the pressure drop across the regenerator as

$$Q'_{viscous} = \frac{\dot{m}_f}{\rho_f L}\frac{dp}{dx} \tag{17}$$

As in the previous equations the spatial coordinate is non-dimensional. For particles the Ergun equation [23] can be used to calculate the pressure drop in conjunction with constants found by Kaviany [24]. Alternatively, experimental data can be used. Due to the magnitude of the pressure drop in the regenerator configurations considered here, the heat leak and eddy current terms are negligible in comparison to viscous dissipation losses.

2.3.2 Regenerator Effectiveness

In addition to the aforementioned parasitic losses, performance is also affected by the effectiveness of the regenerator itself. This includes the efficiency of transferring heat between the refrigerant and the working fluid as well as conduction between the ends of the regenerator.

The conductive component is accounted for in the governing expressions through the non-dimensional conductivity term present in Eqns (5) and (7) and is thus present in both the calculation of enthalpy rate and the differential equation describing the temperature profile. The non-dimensional conductivity is calculated using Eqn (18).

$$\kappa = \frac{\tau_c}{\dot{m}'_s L c_s}\frac{k_{eff} A}{L} \tag{18}$$

where k_{eff} is the effective thermal conductivity of the regenerator.

Because the model assumes perfect heat transfer between the solid and fluid, the effect of convection is removed from the energy balance differential equations. One approach to estimating the impact of finite convection and thermal mass on a regenerator's effectiveness is to relate it to a heat leak from the hot side to the cold side [25]. This approach allows for convection losses on the AMR's cooling power to be post-calculated, without it affecting the temperature profile of the regenerator. Instead, to better approximate imperfect heat transfer in a one-phase passive regenerator model, Vortmeyer proposed converting convection into an equivalent thermal conductivity [26]. This equivalent term combines with the conductive component and explicitly includes the

effects of convection on AMR performance. The effective thermal conductivity can then be written as

$$k_{eff} = k_{cond} + k_{conv} \tag{19}$$

The first term, k_{cond}, takes into account the combined conductivity of the solid and fluid phases in the regenerator. This is calculated using the static component of the thermal conductivity used by Dikeos [17] and Engelbrecht [11]. The dispersive component used in their models, however, is not considered in the single phase approach as it is internally accounted for within the k_{conv} term proposed by Vortmeyer as per [26]. The equivalent convective conductivity is,

$$k_{conv} = \left(\frac{\dot{m}_f c_f}{AR}\right)^2 \frac{d_h}{4h_{eff}\varepsilon} \tag{20}$$

where d_h is the hydraulic diameter, A is the regenerator cross-sectional area, R is the thermal mass ratio and h_{eff} is the corrected convection coefficient. The following empirical correlation derived by Wakao et al [27] describes the convection coefficient for fluids passing through packed beds.

$$h = \frac{\left(2 + 1.1Re_f^{0.6}Pr_f^{1/3}\right)k_f}{d_{part}} \tag{21}$$

where Re_f is the Reynold's number based on the particle size of the porous media, Pr_f is the Prandtl number and d_{part} is the characteristic particle diameter. The convection coefficient is then corrected in Eqns (22) to (26) using a degradation factor to account for internal temperature gradients which may exist in the particles [1][28]

$$h_{eff} = DF\, h \tag{22}$$

$$DF = \left(\frac{1}{1 + \frac{Bi}{5}\phi_H}\right) \tag{23}$$

$$Bi = \frac{hd_{part}}{2k_s} \tag{24}$$

$$\phi_H = \left(1 - \frac{4}{35Fo}\right) \tag{25}$$

$$Fo = \frac{\alpha\tau}{\left(\frac{d_{part}}{2}\right)^2} \tag{26}$$

With the non-dimensional thermal conductivity in Eqn (18) fully defined, the system losses due to regenerator effectiveness are accounted for in the model.

2.3.3 External Losses

The final loss mechanisms in an AMR system are due to effects external to the regenerator. As seen in Figure 2-2 these may include eddy currents in the surrounding materials (for example, the cold heat exchanger), heat leaks from the environment to the cold side due to imperfect insulation and heat leaks from the hot side of the system through the structure. These losses depend on both the device configuration and ambient conditions and can be determined through experimental or numerical means.

Eddy current heating losses can occur within the device due to the presence of the time-varying magnetic field and metallic materials. This is calculated using the following approximation by Kittel [29] for the electrically conducting components subjected to the time varying field [30].

$$Q_{eddy,c} = \sum_{i=1}^{n} \left(\frac{\Gamma A V}{32\rho} B^2\right)_i \tag{27}$$

where Γ is a geometric form factor, A is the area enclosed by the current loop, V is the material volume, ρ is the electrical resistivity, B is the magnetic field change normal to the area and n is the number of parts in the device.

Ambient heat leaks occur throughout the entire refrigeration device and across the regenerator shell. They can occur in piping, heat exchangers or generated through bearing friction. This loss varies depending on the overall design of the device and can be estimated through both modeling and experimental methods. The estimated losses for the AMRTA and PMMR1 devices used in validations are presented in more detail in Chapter 4. However, for completeness, the AMRTA heat leak losses are provided in Eqn (28) below based upon experiments and modeling by Tura [30]. This loss is per

regenerator as shown in Figure 2-2 and needs to be multiplied by the number of AMR's in the device.

$$Q_{amb,c} + Q_{leak} \cong \left(\frac{0.08W}{K}\right)(\mathrm{T_H} - \mathrm{T_C}) \tag{28}$$

With the external losses defined the total cooling power for the regenerator is defined as

$$Q_c = H(x = 0) - Q_{eddy,c} - Q_{amb,c} - Q_{leak} \tag{29}$$

This is multiplied by the number of regenerators to get the cooling capacity for the entire device. Using Eqn (29) and the temperature span defined by Eqn (15), the model can be tested against experimental data.

This chapter began by describing the governing equations for the simplified model. The first equation described a means to calculate three of the four state temperatures within an AMR magnetic cycle assuming that one state is known. The next set of equations was then used to find $T_a(x)$ across the regenerator allowing for the temperature span of the regenerator to be defined from the state points. The internal and external losses present in an AMR system were then defined for an arbitrary device which led to an equation defining the total cooling power. With the numerical formulation of the model defined, the next chapter will discuss its implementation into a programming environment. This primarily includes an interpretation of material data and the magnetic fields in the system for the simplified model. A summary of the inputs and outputs are also discussed.

Chapter 3 – Model Implementation

The AMR model uses the developed theory and correlations in conjunction with material data, geometric parameters and operating conditions to determine the temperature distribution across the AMR. From this, performance parameters such as expected cooling capacity and work input can be determined. Since the regenerator boundary temperatures are an input to the simulation, the temperature span of the regenerator is artificially created. The cooling capacity and work for a given temperature span are then post-calculated. The inputs required for the simulation are discussed next, followed by a more detailed description of the solution process within the model. Outputs from the model will then be discussed in brief.

3.1 Inputs

Operation of the simplified AMR model requires several inputs: material properties, the magnetic field profile and device operating conditions. Material data can be obtained through published works, simulated from known materials or approximated using mean field theory. The field profile can be either assumed or taken from experimental measurements for existing devices. Finally, the operating conditions under which the device is run are required. This includes frequency, utilization, regenerator mass, regenerator dimensions, material diameter and the working fluid in the system. These values depend on the physical device setup and typically require no manipulation. Conversely, material properties and the magnetic field profile need to be discussed further before being implemented into the model.

3.1.1 Material Data

An earlier version of the presented model used *ideal* material properties in the solution of the governing equations [22]. This included a linear magnetocaloric effect with temperature, symmetry between the hot and cold blows, $\sigma = 1$, and the fact that the thermal mass ratios between the hot and cold blows are equal, $R_C = R_H = R$. This analysis is useful for quickly comparing the relative performance of materials and for predicting the general coefficient of performance (COP) or exergetic cooling power of a device. Using real material data is important, however, in determining both the level of accuracy

of the previous simplifications and validating the model with experimental results or other models.

As discussed in the previous chapters, the adiabatic temperature change, ΔT, as a function of temperature and field is essential in computing the temperature span and cooling capacity. For the experimental validations provided in this thesis, the necessary material data was provided by AMES Iowa National Lab for Gd, $Gd_{0.74}Tb_{0.26}$ (GdTb) and $Gd_{0.85}Er_{0.15}$ (GdEr) in the form of specific heat data at multiple field strengths. This specific heat data can be integrated to determine the material's entropy [31] and. subsequently. the MCE for a given change in field strength as described by Eqns (30) and (31).

$$s(T) = \int_0^T \frac{c_B}{T} dT \tag{30}$$

$$\Delta T = T(s_1, B_2) - T(s_1, B_1) \tag{31}$$

The MCE for Gd, GdEr and GdTb from 0 T to 2 T is seen in Figure 3-1. It is important to clarify that a MCE is generated due to any change in field strength, regardless of whether or not the low field is 0 T.

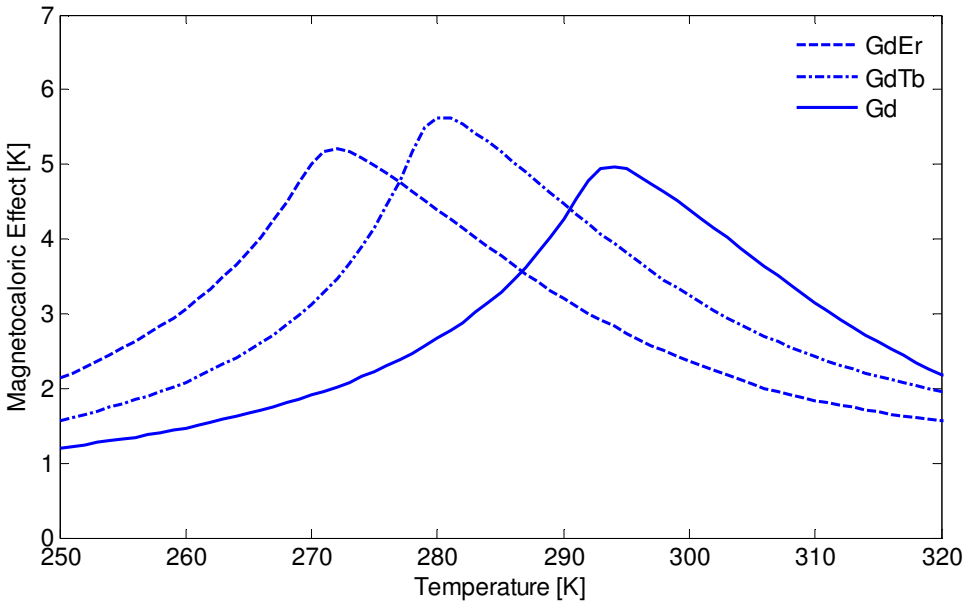

Figure 3-1: MCE of Gd, GdEr and GdTb for a change in field strength from 0 T to 2 T.

In the case of Gd, specific heat data is available for a large number of different field strengths. This data is interpolated in MATLAB using the TriScatteredInterp function allowing for the adiabatic temperature change to be found at any desired temperature or between any field strengths (up to 7 Tesla). This is particularly useful for experimental validation where the high and low field strengths can vary greatly. In the case of the GdEr and GdTb alloys, however, material data is only available at 0 T and 2 T. Due to the highly non-linear nature of specific heats with temperature and field, this data alone prevents one from being able to accurately predict the MCE under any other field conditions. To overcome this, the MCE and Curie temperatures of GdEr and GdTb can be found at 2 T and used to vertically scale and horizontally shift the interpolated Gd data, respectively. This is due to the similarities in the shape of second-order material data as demonstrated by Figure 3-1.

This same technique is also used in the simulation of materials. Instead of the MCE and Curie temperature being taken from other material data, though, these values can be chosen by the user to shift the interpolated Gd data as needed. This simulated material is then useful for studying the effects of layering regenerators without being hindered by the availability of existing materials or material data. Other materials simulated using this approach include GdPd, $GdNi_2$, and $DyAl_2$ [32]. These materials have Curie temperatures below 80 K and are relevant in cryogenic applications of magnetic refrigeration.

The magnetocaloric effect for each of these materials can now be found for a wide range of high and low field choices. To compare the model with experiments, the representative field strengths experienced by the materials must be determined.

3.1.2 Magnetic Field Profile

The magnetic field required for an AMR refrigerator is generated through either superconducting coils or permanent magnets. Peak high and low fields are then generated in the magnetocaloric material by moving the regenerator and the magnet relative to one another. In the devices considered in this thesis, the magnetic field experienced by the magnetocaloric material varies sinusoidally over a cycle as shown in Figure 3-2. An accurate numerical representation of a magnetic cycle then requires a

magnetocaloric effect that varies over the period of a cycle. The simplified numerical model, however, is derived assuming the magnetic field behaves like an on-off switch containing only a single low and high field value during each of the fluid blows as shown in Figure 1-4. Thus, a method for determining an effective high and low field, which would produce a MCE representative of the physical system, is needed.

Choosing the peak values of the experimental magnetic profile for the model would overestimate the magnetocaloric effect and subsequently the device performance. Instead, the RMS values of the fields during a blow period are used. This requires a full cycle to be broken into two sections. The high field portion of the magnetic profile occurs for the first half of the cycle as seen in Figure 3-2 and corresponds to a hot blow of fluid through the regenerator. The low field portion is the latter half of the cycle and corresponds to the cold blow. The RMS fields for a 2 T sinusoidal field are shown in Figure 3-2. The model also provides the option of adding demagnetization effects by scaling the calculated RMS fields.

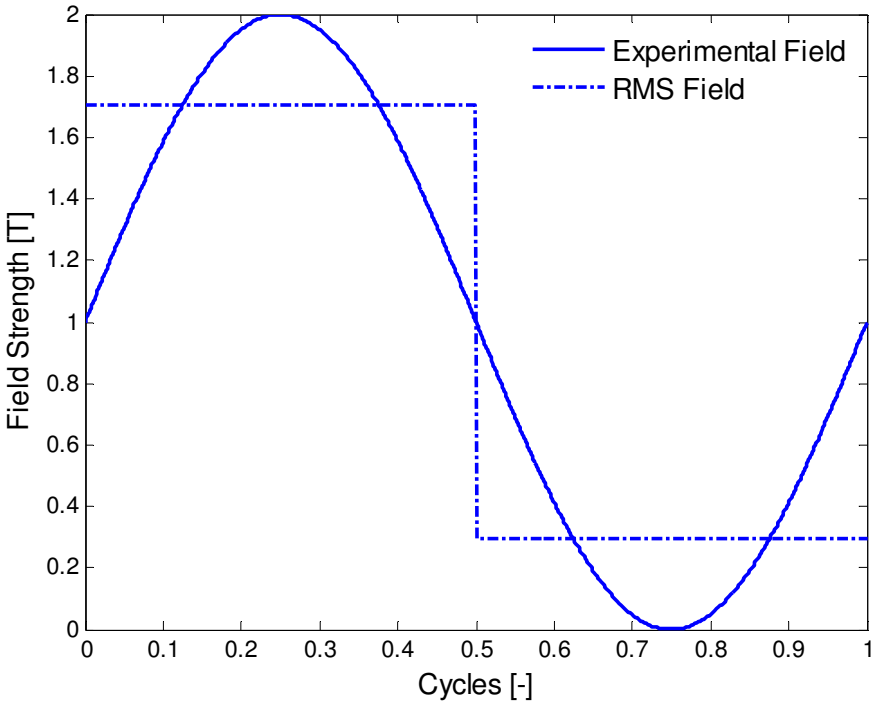

Figure 3-2: Example of a sinusoidal field profile with an RMS approximation for the high and low field values.

Device specific parameters such as the field profile and system losses can also be pre-programmed into the model's database so that a user only needs to select an existing device.

3.2 Model Operation

With the system inputs defined, the simplified model can be used to determine an AMR's performance. This solution is obtained using several MATLAB functions. The first function determines the effective high and low field strengths from the field profile and determines the MCE and specific heat values of the material between those RMS fields. In the case of layered regenerators, this function passes on the properties of all materials present in the regenerator. Another function, REFPROP, developed by the National Institute of Standards and Technology, determines the working fluid's properties using the type of fluid, system charge pressure and a reference temperature. This reference is chosen as the average of the boundary conditions T_{a0} and T_{a1}. For the conditions considered, fluid properties are not overly sensitive to temperature, and a single reference temperature for properties is considered sufficient. The inputs and outputs of those functions are expressed in Figure 3-3.

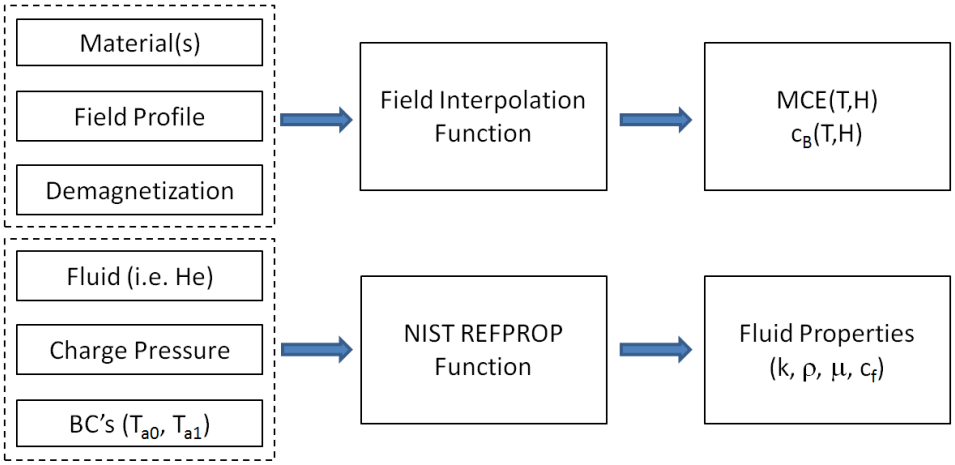

Figure 3-3: Inputs and outputs of the Field Interpolation and REFPROP functions.

Using the calculated and pre-set system parameters, the regenerator's temperature distribution, $T_a(x)$, is determined from Eqn (13) using a discrete number of points. This equation is solved along the entire domain using MATLAB's bvp5c ODE solver in combination with the user-specified boundary conditions $T_a(x=0)$ (T_{a0}) and $T_a(x=L)$ (T_{a1}).

Solution of this equation requires multiple iterations as several of the terms in the ODE are temperature dependent. The MATLAB solver automatically increases the mesh size of the system to a point where the solution is mesh independent to within a relative error of 0.1 %. Reducing the error tolerance further has no effect on the tested simulations.

For multilayered regenerators the multipoint boundary conditions option within bvp5c is used. This allows for the differential equation to be split into different regions along the length of the simulated regenerator. Each region then represents a different material with its own properties including MCE, specific heat and utilization. The differential equation is then solved with the additional intermediate conditions that the temperature and its first derivative are continuous between material layers. Choosing the length of each region is also straightforward making the weighting of different regions simple to do in simulations.

With $T_a(x)$ computed, the other three state points are found using knowledge of the magnetic cycle [8]; this allows for the average fluid temperature to be calculated from Eqn (15). Cooling capacity is then found using the theory described in the preceding chapter. This requires eddy current and ambient losses that are specific to the device being simulated. Other useful parameters such as magnetic work, pumping power, efficiency and COP can also be post-calculated using the temperature profile and cooling capacity. Inputs and outputs for the differential equation are shown in Figure 3-4.

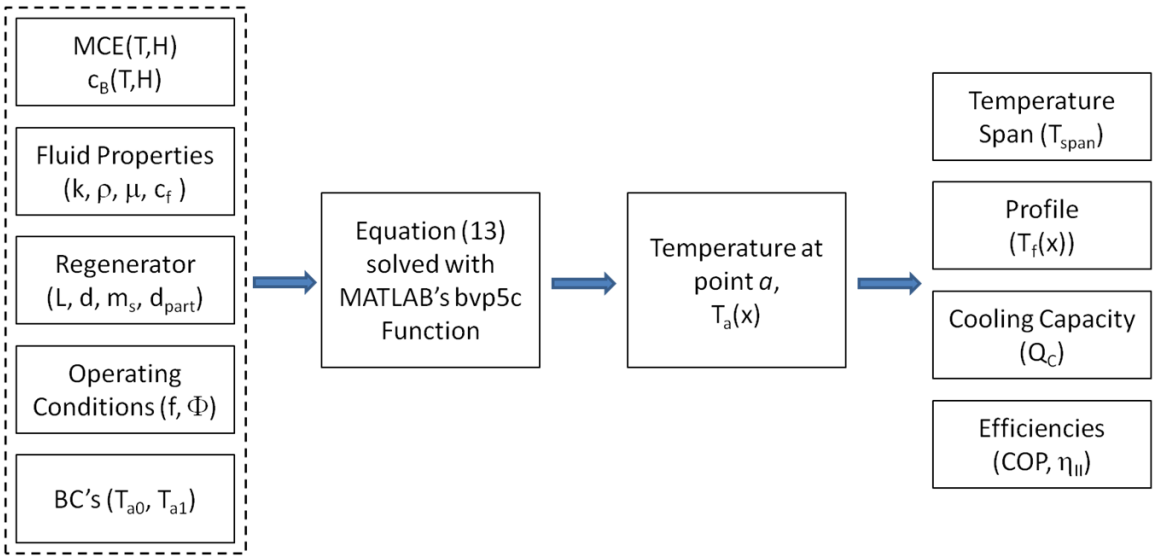

Figure 3-4: Inputs and outputs of the AMR differential equation.

Since the boundary conditions required for the model are in the form of a temperature at point *a* in the magnetic cycle, the choice of boundary conditions influences the outputs. For example, choosing boundary conditions only a few degrees Kelvin apart will result in a relatively low temperature span but a high cooling capacity. Experimental results, on the other hand, may characterize the device performance under a no load condition (Q_c = 0). Acquiring simulated results corresponding to experimental data points may then require multiple simulations to be run and the data interpolated. For this reason, multiple scripts were created to automatically adjust the boundary conditions between simulations until the desired performance curve is achieved. The model takes approximately 2 s to solve for a single set of boundary conditions on a laptop computer with a 2.40 GHz Intel® Core™ i5 processor. To plot a T_H vs T_{span} curve with a sufficient number of points, like the ones seen in the validation section, requires between 1 and 3 minutes depending upon the operating conditions.

3.3 OUTPUTS

Outputs from the model include the temperature span and distribution through the regenerator, cooling capacity, work inputs and efficiencies. These values can be used for comparison to experimental results or for a multitude of research applications including optimization programs, costing and regenerator design. Figure 3-5 shows a sample output of the four temperatures in the magnetic cycle (see Figure 1-4) using Gd with a field variation from 0 T to 2 T.

A similar output, seen in Figure 3-6, can be produced for a multilayer regenerator composed of Gd, GdTb and GdEr for a field of 0 T to 2 T. In this case the temperature profile differential equation uses the multipoint boundary conditions, as described in the previous section, resulting in $T_a(x)$ having a continuous profile across the regenerator. The other three curves, however, have discontinuities as they are post-calculated and use the respective MCE's of the individual materials. This effect is unavoidable in a time independent model as only the steady state solution can be calculated. As shown in the following section this method is still capable of replicating experimental trends with a sufficient level of accuracy.

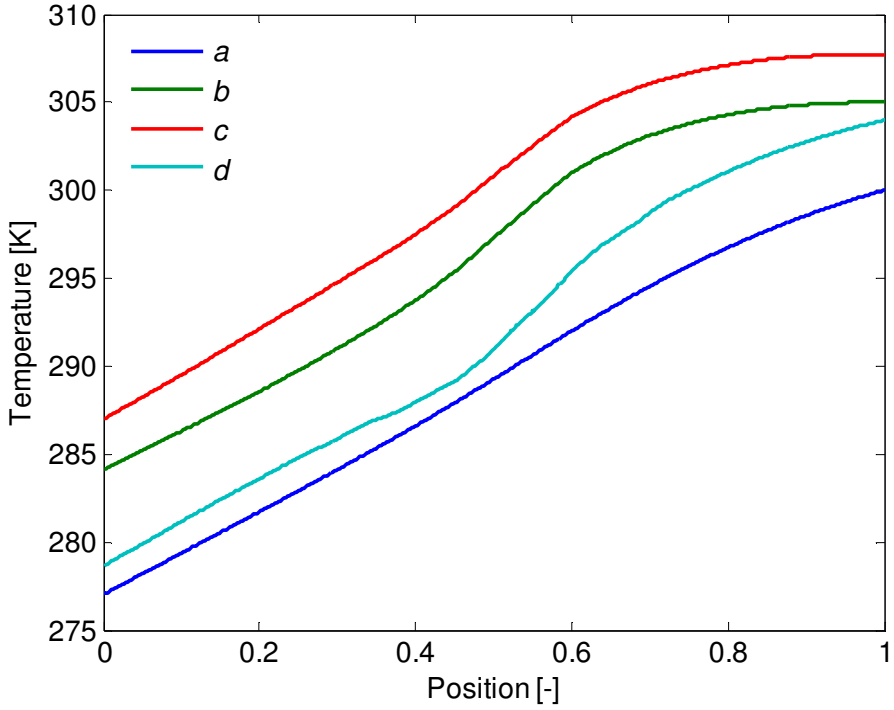

Figure 3-5: Sample output of the fluid temperatures for Gd, $\Phi = 0.29$ and $R = 1.0$ across the regenerator.

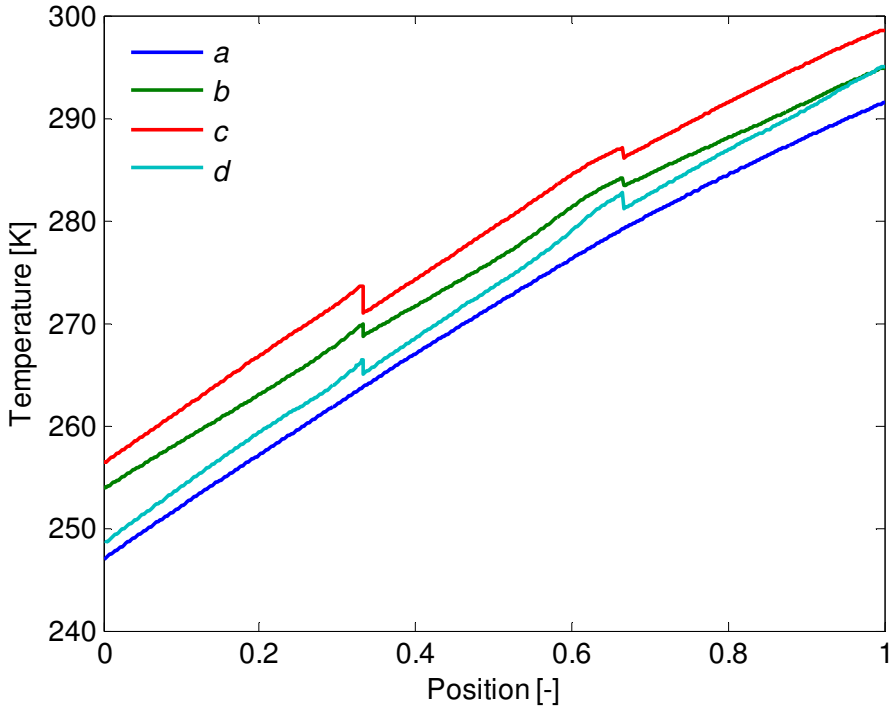

Figure 3-6: Sample output of the fluid temperatures for Gd-GdTb-GdEr, $\Phi = 0.10$ and $R = 1.0$ across the regenerator.

It is also important to note that the functional outputs of an AMR model vary depending upon the application. For example, when evaluating the performance of materials or regenerator configurations, the hot end temperature, T_H, temperature span, T_{span}, and cooling capacity, Q_c are of primary interest. These three values allow for two important curves to be created: Q_c versus T_{span} for a fixed T_H, and T_{span} versus T_H for a fixed Q_c. These curves are used in Chapter 4 for experimental validation. Efficiency, COP and work outputs are primarily important when comparing the overall designs of devices or running cost optimization programs. These types of analyses typically require the input parameters to be varied over a large space in order to determine an optimal operating point. It is these applications where the simplified model is most useful due to the low computational time relative to higher-order AMR numerical models.

This chapter discussed the implementation of the simplified model into a programming environment. A method for simulating materials based on Gd data was developed due to the similarities in the properties of second-order refrigerants. RMS values were also used to represent a sinusoidally varying field to fit the model's requirement of a single high and low field strength. The MATLAB functions which convert the raw material data and operating conditions into a predicted temperature span and cooling capacity were then described. Sample outputs of the model were then shown for single and multilayer regenerators. The model will now be used to simulate plots using the same operating conditions as two experimental devices for the purpose of comparing the results. This will provide a measure of validation for the model.

Chapter 4 – Model Validation

Before a numerical model can be used as a predictive tool for research applications, the results have to be validated. A model should be able to follow both the general trends and the sensitivities associated with varying parameters. Ultimately, a level of confidence needs to exist in simulated results if a model is to be a useful asset in studying magnetic refrigeration technology. Experimental results used in the validation procedure include data from a superconducting AMR test apparatus (SC-AMRTA) [10] and a permanent magnet magnetic refrigerator (PMMR1) [33] both constructed at the University of Victoria. These devices use different working fluids and magnetic waveforms allowing for the model to be tested over a relatively large operating space.

4.1 Active Magnetic Regenerator Test Apparatus

The SC-AMRTA device at the University of Victoria uses a superconducting magnet to produce magnetic fields up to 5 T. It utilizes a two regenerator system that is moved in and out of the magnetic field using a crank mechanism and operates similar to the one described in Figure 1-5 but with a stationary magnet.

The type of performance parameters used for validation include the temperature span across the regenerator, T_{span}, at a given hot end temperature, T_H, for a specified heat load or cooling capacity, Q_c. These parameters vary greatly depending upon the regenerator materials, utilization, heat load and frequency, making it a good set of data to compare against the model. A summary of the fixed and variable parameters used within the experimental data set are shown in Table 4-1.

Table 4-1: Temperature independent parameters of the superconducting AMRTA experiments.

Test Parameters	
Frequency (Hz)	0.65 - 0.8
Stroke Length (m)	0.21
Effective Displacer Area (mm^2)	2513
Regenerator	
Material Mass (g per puck)	40-45
Porosity	~55%
Length (mm per puck)	25
Diameter (mm)	25
Characteristic Particle Diameter (μm)	560
Particle Type	Crushed particles
Number of Regenerators	2
Magnetic Material (Gd)	
Thermal Conductivity ($W K^{-1}$)	10.3
Density ($kg m^{-3}$)	7900
Reference Specific Heat ($J kg^{-1} K^{-1}$)	381
Working Fluid (Helium)	
Pressure (atm)	3 - 9.7

The regenerators are made of crushed particles which are formed into pucks containing between 40-45 g of magnetocaloric material each. Regenerators in these experiments are composed of one, two or three pucks made from Gd, GdEr or GdTb and can be seen in Figure 4-1 [10]. The magnetic field used for all of the tests is 2 T.

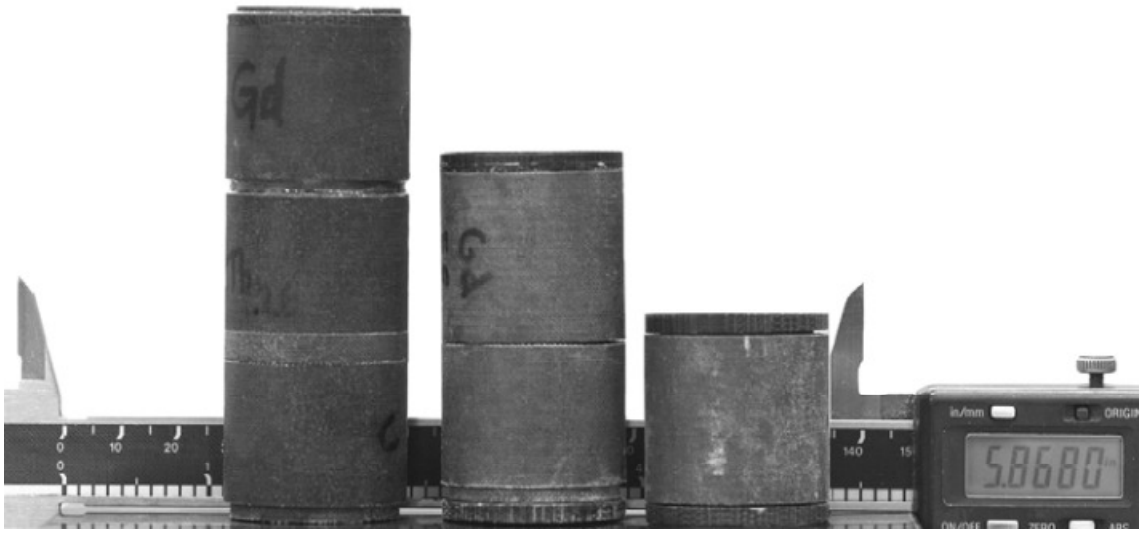

Figure 4-1: Picture of the regenerator pucks used in the AMRTA experiments.

4.1.1 Device Specific Parameters

As described within Chapters 2 and 3, several of the inputs required for the numerical model are device dependent. These include the magnetic waveform, ambient heat leaks and eddy current losses. In the AMRTA, the magnetic profile experienced by the regenerators is a sine wave with a peak field of 2 T and a minimum of 0 T as shown in Figure 3-2. This subsequently produces high and low RMS field strengths of 1.707 T and 0.293 T, respectively. Because the superconducting field passes axially through the regenerator beds, demagnetization effects are ignored in this case. This may not be the case for regenerators that are operating high above their Curie temperatures and hence begin behaving like a paramagnet.

The AMRTA heat leak and eddy current losses were also estimated by Tura et al [30]. Eddy current losses in the AMRTA components, which have direct impact on the cooling capacity (i.e. cold heat exchanger), are negligible while an ambient heat leak per regenerator due to friction is shown in Eqn (28). Since the particles used in the regenerator are irregular and not easily represented using Ergun's equation, experimental pressure drops recorded by Tura are used in the analysis [10].

4.1.2 Results

A variety of experimental conditions are evaluated to ensure the model is tested in more than a single operating region of the AMR. As such, the following results vary by material type, material mass, utilization, frequency and heat load.

Figure 4-2 compares the model results to single pucks of Gd, GdTb and GdEr and under no-load (Q_c = 0W) conditions. In all three data sets the model predictions follow the same general trend as the experimental data. The primary discrepancy exists at high T_H values relative to the Curie points where the temperature span begins to drop more rapidly (best seen for GdTb) than experimental data.

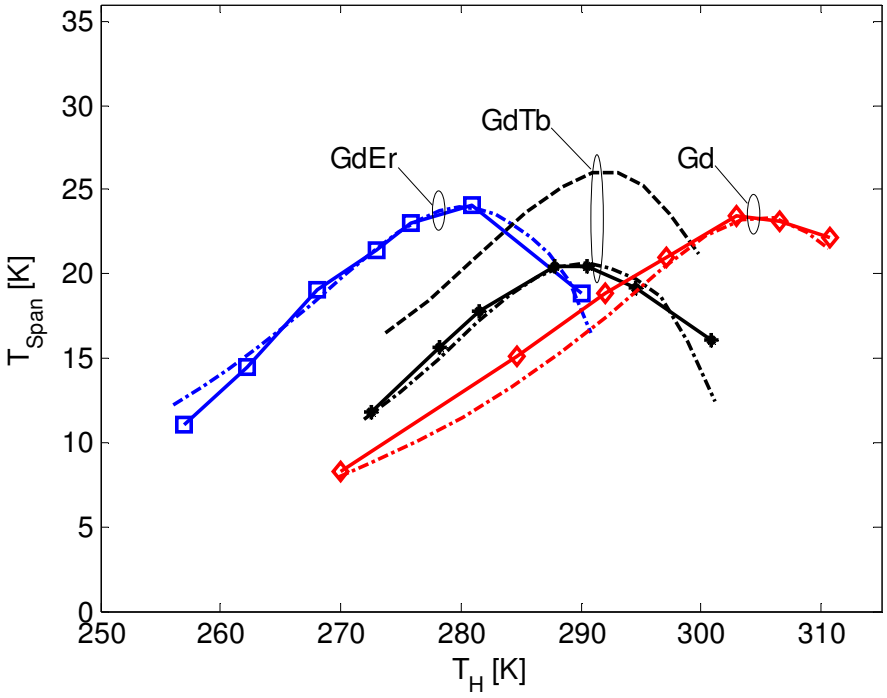

Figure 4-2: T_{Span} vs T_H for single pucks of Gd, GdTb and GdEr at Q_C = 0W. Solid lines represent experimental data while dashed lines are simulations from the model. In the case of GdTb pucks the temperature span is plotted using both original material data and data altered to reduce the MCE.

While the general trends are correct for all three materials, the model tends to significantly over-predict the performance of the GdTb regenerator. As can be seen from the GdTb plots, decreasing the assumed magnetocaloric effect for this material by a factor 0.77 as compared to the raw data corrects the prediction. This is discussed further in Chapter 6 of this thesis.

The model predictions can also be compared to layered regenerators where experimental data is available for two and three layer regenerators using Gd, GdEr and GdTb. Based on the results for the single GdTb bed, the corrected adiabatic temperature change (0.77 scaling) for this material is used in the model. Figure 4-3 demonstrates that the model predicts both the layering aspect and the combination of materials relatively well. The model tends to be less accurate the more the operating temperature is increased above the average Curie temperature of the materials in the bed and as the utilization decreases. Because the gas displaced through the regenerator is constant and adding a material increases the overall regenerator mass, the utilization decreases from ~0.3 for the

single puck experiments down to ~0.1 for the three material tests. For utilizations below ~0.15 the non-dimensional thermal conductivity within the temperature profile differential equation (Eqn (13)) has to be increased by a factor of three for a solution to be found for temperatures above the highest Curie point in the bed. This has little influence on the magnitude of the predicted temperature span but increases the solvable range of the model for low utilization systems.

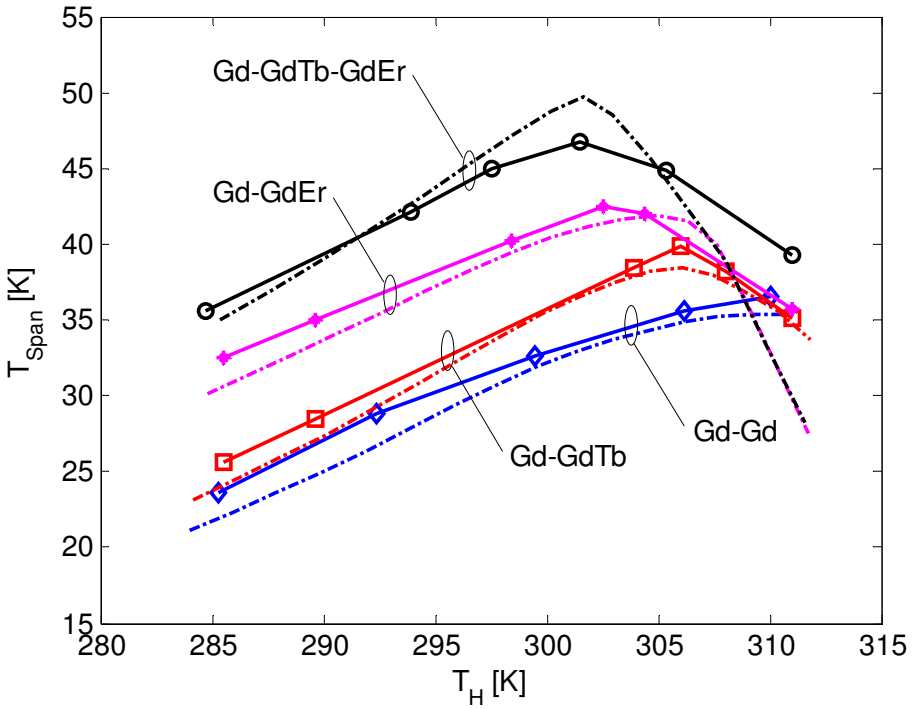

Figure 4-3: T_{Span} vs T_H for two and three puck multilayered regenerators at Q_C = 0W. Solid lines represent experimental data while dashed lines are simulations from the model. Note the vertical axis is offset from 0 K for clarity.

The sensitivity of the temperature span to an applied thermal load is shown in Figure 4-4 for a single Gd puck at 292K and 305 K. From Figure 4-4a, the experimental results are in good agreement with the model. The model has been used to also show the effect that system losses have on the predicted cooling capacity. Recalling Eqn (29), the net cooling power is determined by the enthalpy flow at $x=0$, $H(x=0)$, less the parasitic heat leaks from ambient, $Q_{amb,c}$, and from the hot side of the system, Q_{leak}. The impacts of regenerator thermal ineffectiveness, internal losses and the external losses can be easily shown. In this case, internal losses are due to viscous dissipation. The top curve represents the temperature span for a system with perfect regenerator effectiveness (κ =

0), no viscous dissipation and no ambient cooling losses. Below this curve is the same scenario but with regenerator ineffectiveness included. The next curve then shows the cooling power when only the external losses are excluded while the final solid curve accounts for all system losses and is the predicted cooling capacity for the device. This analysis of system losses is important in optimization studies for determining where experimental devices can be improved and potential effects these improvements have on the temperature span and cooling capacity. As seen when comparing Figure 4-4a and Figure 4-4b, viscous dissipation losses are more significant at higher hot end temperatures.

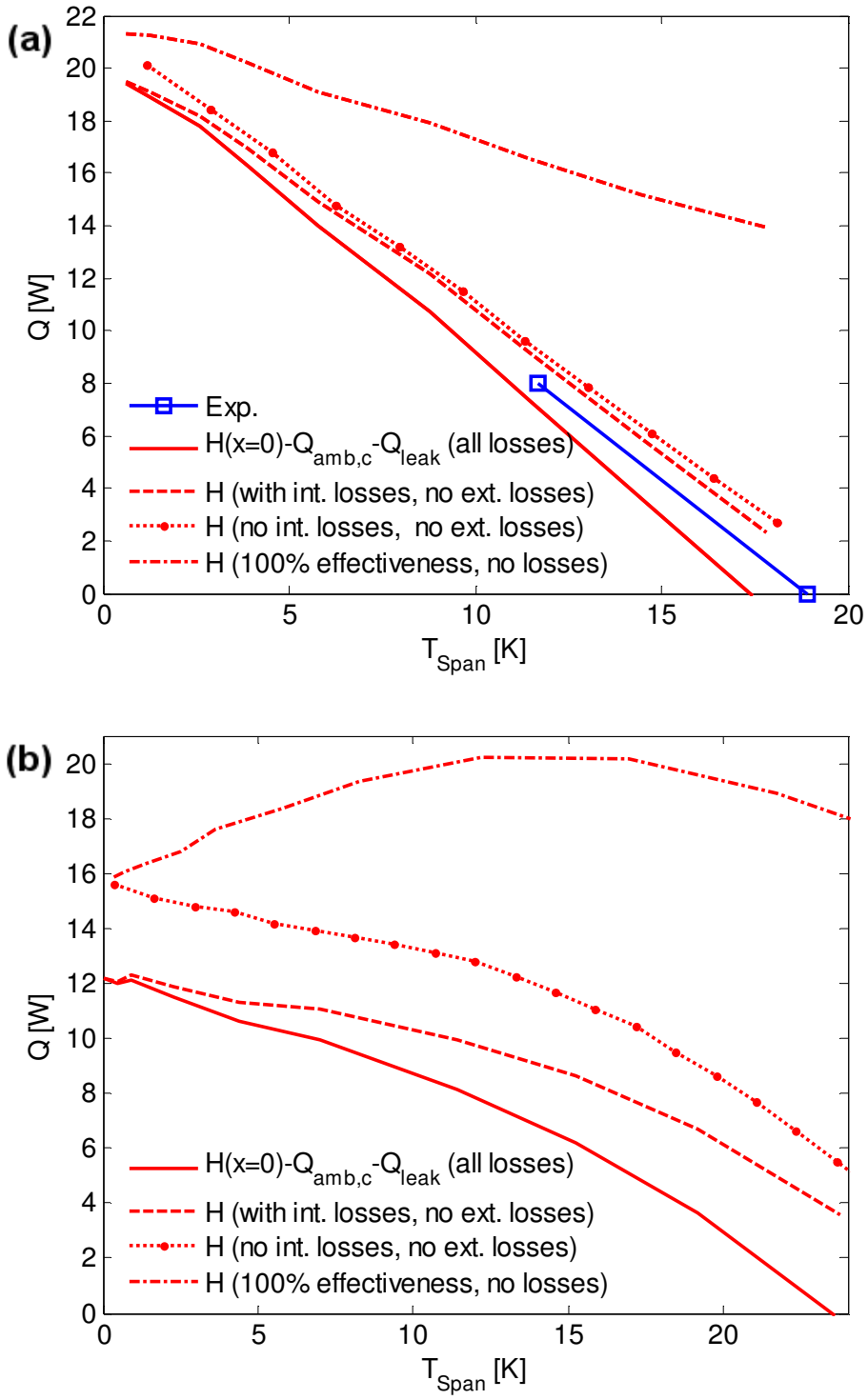

Figure 4-4: Q_c vs T_{Span} for single-pucks of Gd at 0.65Hz, (a) T_H = 292K and (b) T_H = 305K. The effects that internal and external losses have on the cooling capacity and temperature span are shown. The difference in the impact of viscous dissipation (internal losses) is also shown between the two plots.

In Figure 4-5, the temperature span is plotted against three different T_H values for two heat load cases, 0 W and 6 W. In this case the frequency is 0.8 Hz instead of the 0.65 Hz in the previous tests. While both data sets follow the trend of the experimental curve, the model under-predicts experiments at the higher frequency. Potential causes of differences between model predictions and experiments are discussed in Chapter 6.

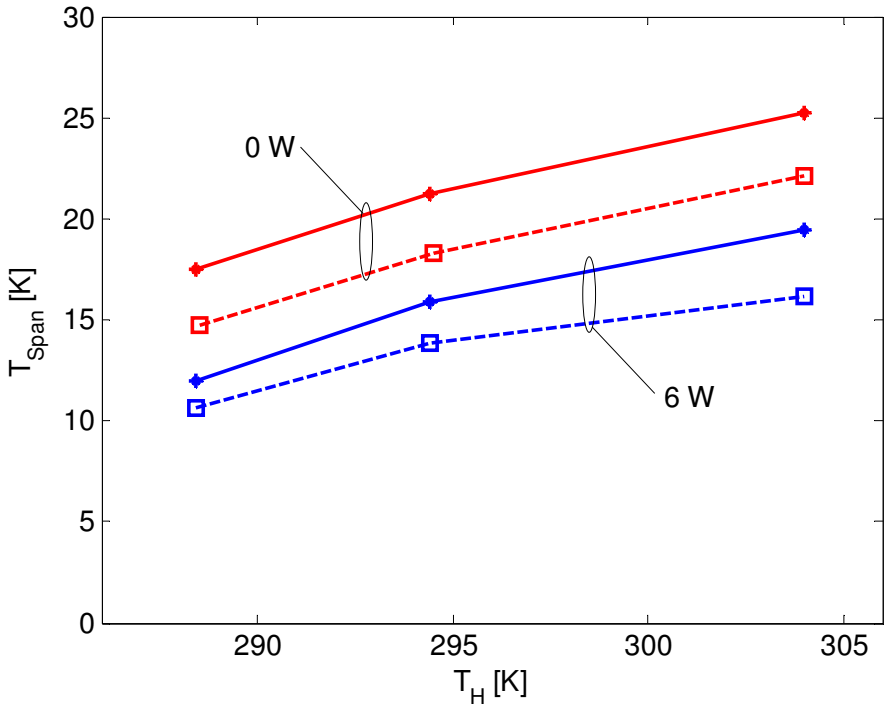

Figure 4-5: T_{Span} vs T_H for single-pucks of Gd at 9.5atm, 0.8Hz and varying load. Solid lines represent experimental data while dashed lines are simulations from the model.

The final experimental result for the AMRTA accounts for a variation in the utilization. For the AMRTA, utilization is varied by altering the pressure of the helium in the system, thereby changing the density and subsequent thermal mass of the displaced fluid. Increasing the utilization raises the pressure drop in the system and, in the case of the AMRTA, increases the temperature span achievable by the regenerator up to certain values. Shown in Figure 4-6 are the temperature span curves at three different charge pressures, or utilizations. Similar to the heat load sensitivity curves in Figure 4-5, the temperature span follows the experimental trends. Furthermore, at a pressure of 3 atm, the temperature span is trending lower at 304 K.

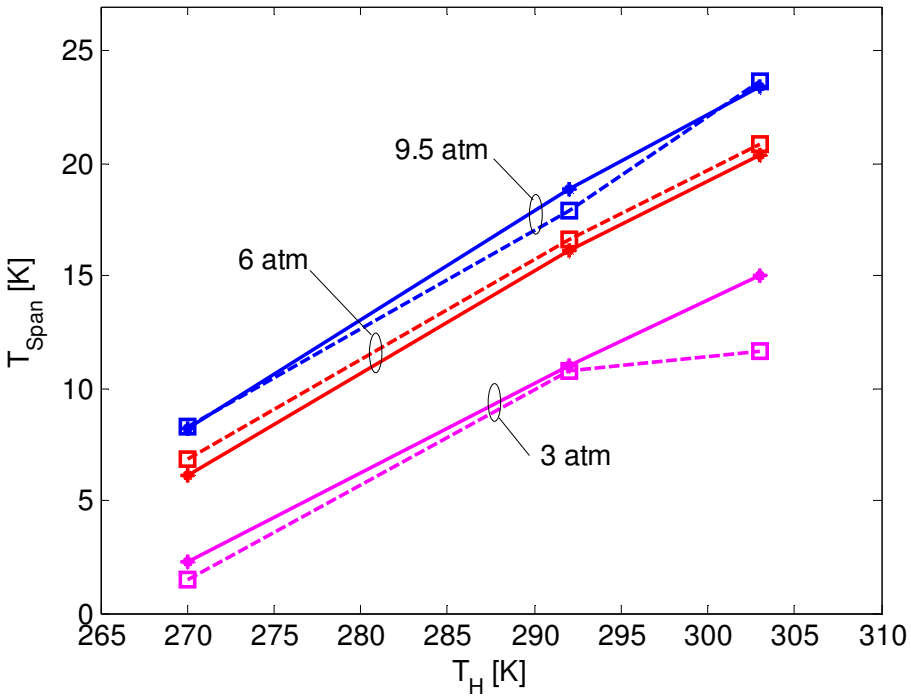

Figure 4-6: T_{Span} vs T_H for single-pucks of Gd at 0.65Hz, Q_C = 0W and varying utilization (charge pressure). Solid lines represent experimental data while dashed lines are simulations from the model.

4.2 Permanent Magnet Magnetic Refrigerator

Unlike the AMRTA, which uses a stationary superconducting field to magnetize the regenerators, the PMMR1 device uses rotating permanent magnets. The field felt by the regenerator bed is varied by the rotation of two concentric cylinders containing the permanent magnet material. This configuration, called a nested Halbach array, allows for a much higher operating frequency in the device which then increases cooling power [33]. As with the AMRTA validations, T_H vs T_{span} curves at different cooling loads are used for comparison of the results. A summary of the fixed and variable parameters used within the experimental data set are in Table 4-2.

Table 4-2: Temperature independent parameters of the PMMR1 experiments.

Test Parameters	
Frequency (Hz)	2 - 4
Displaced Volume (cm^3)	3.1 – 6.4
Regenerator	
Material Mass (g)	55.3
Porosity	~35%
Length (mm)	55
Diameter (mm)	15.8
Characteristic Particle Diameter (μm)	300
Particle Type	Spheres
Number of Regenerators	2
Magnetic Material (Gd)	
Thermal Conductivity (W K^{-1})	10.3
Density (kg m^{-3})	7900
Reference Specific Heat (J kg^{-1} K^{-1})	381
Working Fluid (Water-Glycol: 80/20)	

The regenerators for all of the PMMR1 tests are 55.3 g of 300 μm Gd spheres packed into cylindrical tubes; thus, tests compare impacts of operating parameters.

4.2.1 Device Specific Parameters

Much like the superconducting device the magnetic profile and cycle losses need to be quantified specifically for the PMMR1 device. In this case, however, the magnetic field felt by the regenerator is more complicated than the AMRTA setup. Due to the finite length of the concentric permanent magnets, the magnetic field varies across the length of the regenerator, eventually reducing to zero once outside the bore of the magnets. This means that the average peak magnetic field across the regenerator depends on the regenerator length. For this analysis, the model will assume that the entire bed is uniformly magnetized and demagnetized, meaning a single average peak field is needed for calculations. The average peak field for 55 mm and 90 mm long regenerators are shown in Figure 4-7 along with the experimental peak field in the bore of the magnets.

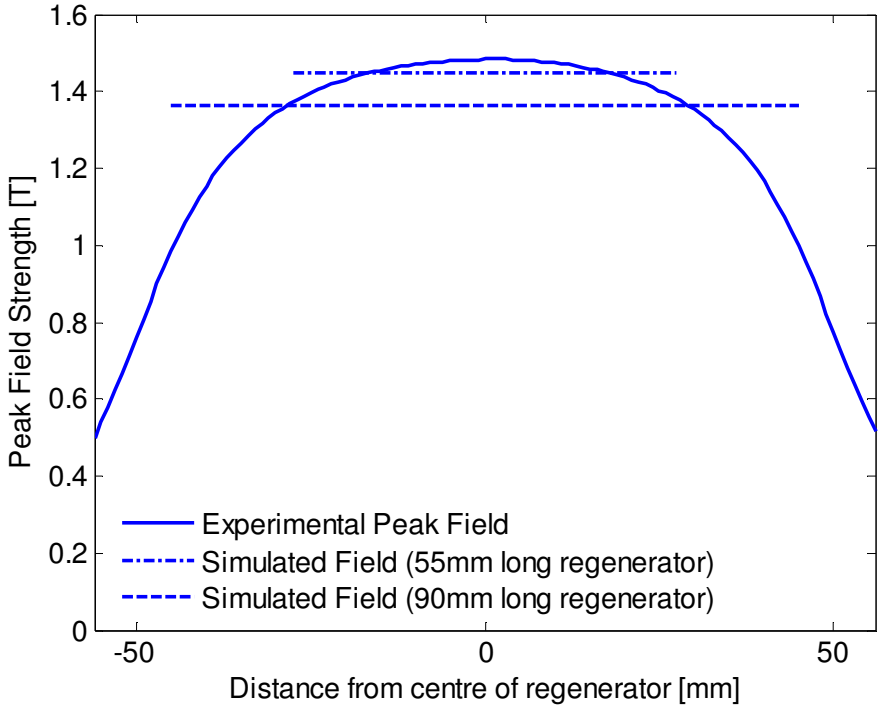

Figure 4-7: Plot showing the change in peak field along the axial length of the regenerator.

Using the experimental data, the following fourth degree polynomial is created to represent the average peak magnetic field as a function of regenerator length for use in the model.

$$H_{peak} = -2200L^4 + 236L^3 - 20.4L^2 + 0.211L + 1.482 \quad (32)$$

where L is the bed length in m and H_{peak} is in T. For the 55 mm regenerators used in the experiments, this gives a peak field of 1.451 T.

The magnetic waveform over a cycle with a peak of 1.451 T is then plotted in Figure 4-8 where one cycle represents a full rotation of the concentric magnets. This waveform is similar to a squared sine wave shifted vertically by 0.1 T. The RMS values for the high and low fields are calculated and plotted with the original waveform.

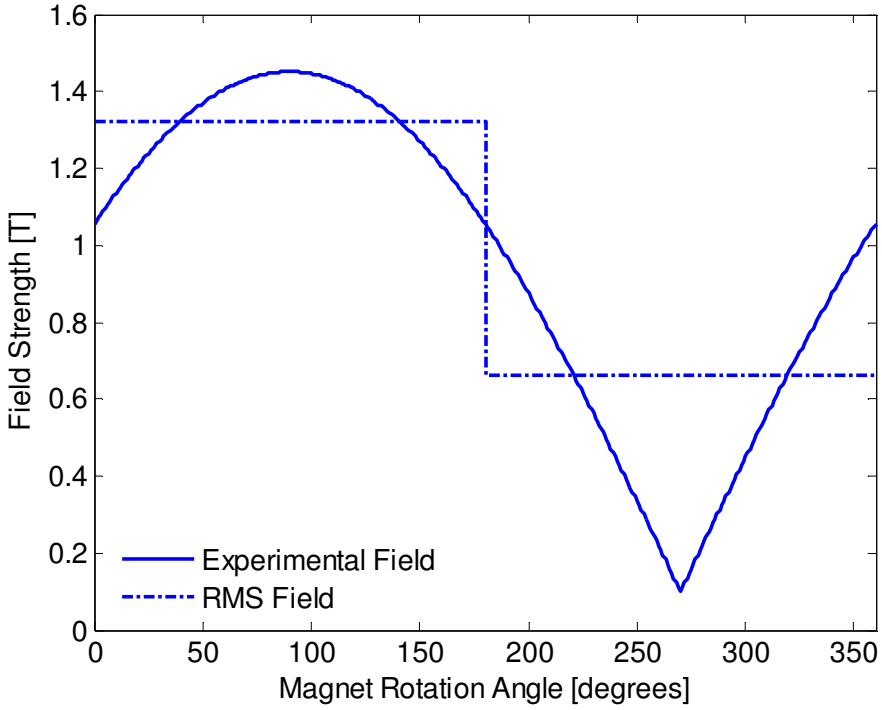

Figure 4-8: Experimental and RMS fields for the PMMR1 device with no demagnetization.

Since the magnetic field penetrates the regenerator along its radius, some demagnetization effects occur due to geometry. Modeling results showed this demagnetization to be approximately 24 %[1]. Using a demagnetization of 29 %, however, produces a better fit with the experimental data in terms of the curvature of the temperature span curves. The high and low RMS fields used for validation are subsequently 1.130 T and 0.663 T, respectively.

Similar to the AMRTA, losses due to eddy currents are found to be negligible. Heat leaks to the system were approximated both experimentally and modeled using COMSOL with similar results[2]. The heat leak through the regenerator shell is estimated in Eqn (33) while the ambient heat leak from the cold heat exchanger is described by Eqn (34). Again, the losses in Eqns (33) and (34) are per regenerator meaning that the losses are multiplied by two in the simulations for the PMMR1 device.

$$Q_{leak} \cong \left(\frac{0.054W}{K}\right)(\mathrm{T_H} - \mathrm{T_C}) + 0.0019 \tag{33}$$

1. Demagnetization results for the PMMR1 device modeled by Alex Ruebsaat-Trott
2. Heat leak modeled by Alex Ruebsaat-Trott and experimentally tested by Oliver Campbell

$$Q_{amb,c} \cong \left(\frac{0.142W}{K}\right)(\mathrm{T}_\infty - \mathrm{T}_\mathrm{C}) + 0.0297 \tag{34}$$

4.2.2 RESULTS

Validations for the PMMR1 device are performed at 2 and 4 Hz for four different experimental utilizations: 0.62, 0.94, 1.03 and 1.28. The utilization is varied by adjusting the displaced volume of fluid through the system. For the utilizations of 0.62, 0.94, 1.03 and 1.28, this corresponds to displaced volumes of 3.1, 4.75, 5.15 and 6.4 mL, respectively. This displaced volume is produced using three different sized displacers with variable stroke lengths.

The model simulations for seven different scenarios are shown in Figure 4-9 through Figure 4-12. When comparing the results, three aspects are considered important: the overall magnitude of the curves, the sensitivity of the temperature span to an applied heat load and the curvature of the results. Although the simulations match the general trend of the experimental curves, both the magnitude of the load curves and sensitivity to heat load is different in most cases. This discrepancy is larger for the 4 Hz experiments, particularly for utilizations of 0.94 and 1.03. With the exception of a utilization of 0.62, the 2 Hz simulations predict the experiments to within a few Kelvins. For the simulations the Curie point of Gd is decreased by 4 K to align the trends of simulated results with the experimental curves.

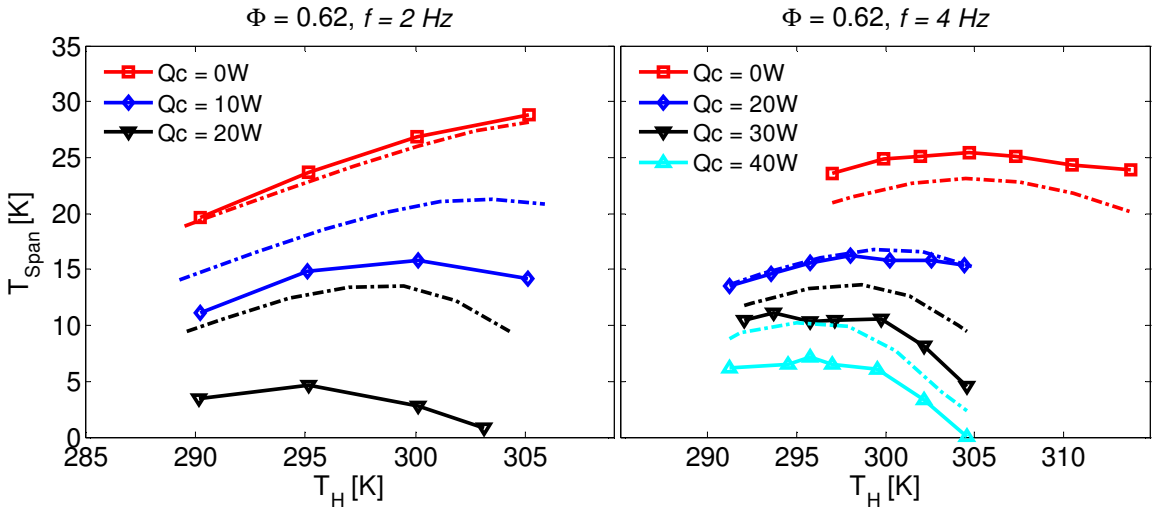

Figure 4-9: PMMR1 load curves at frequencies of 2 Hz (left) and 4 Hz (right) and $\Phi_{calc} = 0.62$. Solid lines represent experimental data while dashed lines are simulated results.

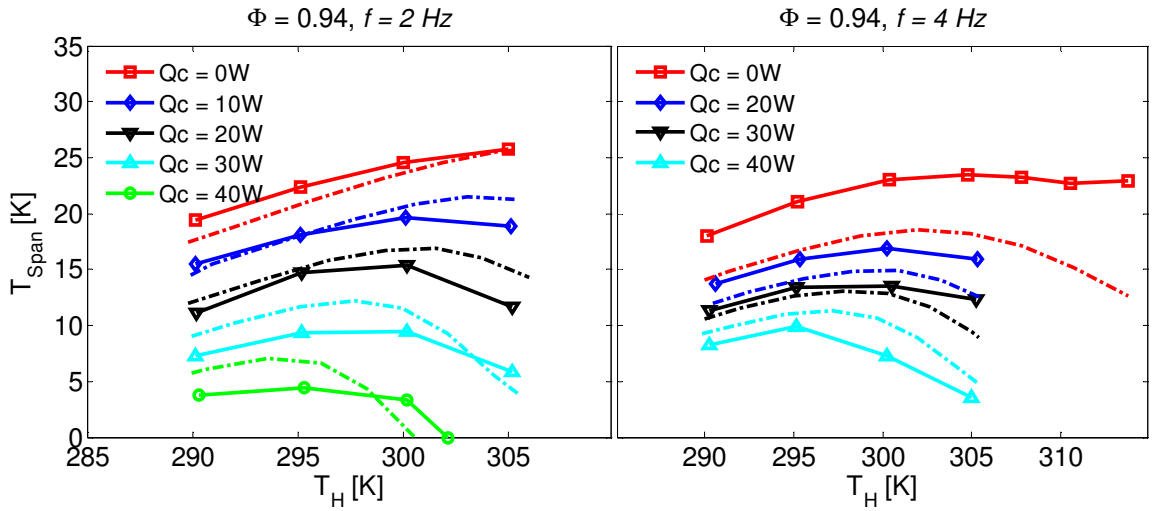

Figure 4-10: PMMR1 load curves at frequencies of 2 Hz (left) and 4 Hz (right) and Φ_{calc} = 0.94. Solid lines represent experimental data while dashed lines are simulated results.

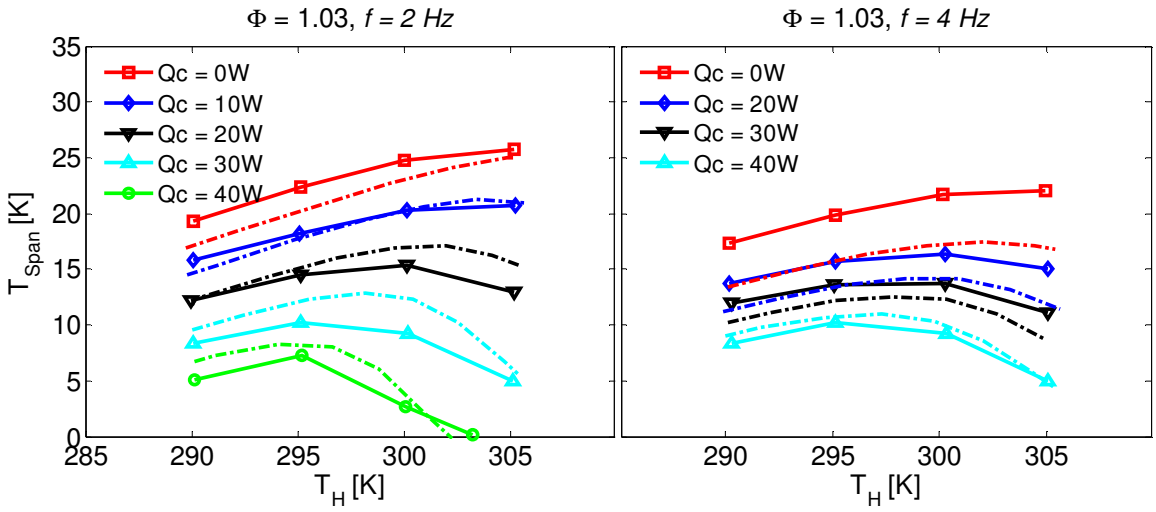

Figure 4-11: PMMR1 load curves at frequencies of 2 Hz (left) and 4 Hz (right) and Φ_{calc} = 1.03. Solid lines represent experimental data while dashed lines are simulated results.

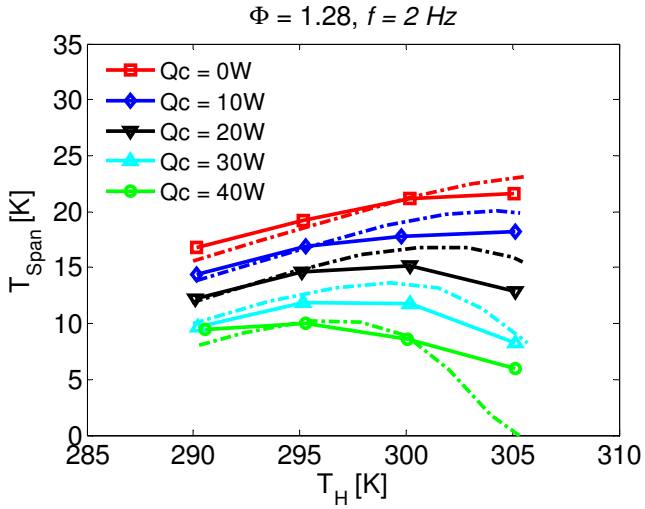

Figure 4-12: PMMR1 load curves at a frequency of 2 Hz and Φ_{calc} = 1.28. Solid lines represent experimental data while dashed lines are simulated results.

In an attempt to improve the agreement between the simulated and experimental results, the effects of varying three different parameters are examined. These parameters are thermal conductivity, high and low magnetic fields and displaced volume. In order for an adjustment to be considered beneficial the simulated results must improve in magnitude and heat load sensitivity relative to the experiments without deviating from the good agreement in curvature seen in the previous simulations.

It is found that varying the thermal conductivity can be used to scale the magnitudes of the simulated curves due to its effect on the regenerator's effectiveness. This approach, however, has little to no effect on the heat load sensitivity for the experimental scenarios. Manually adjusting the high and low magnetic field strengths, on the other hand, allows for both the magnitude and heat load sensitivity of the temperature span curves to be controlled. However, to align the results for each of the seven cases required seven different sets of magnetic fields making this approach unrealistic. Additionally, altering the magnetic field from the calculated values in Section 4.2.1 significantly changes the shape of the temperature span curves; in particular, it creates a sharper and shorter peak than the experimental curves. The final modification tested is a reduction in the displaced volume of fluid within the system. Varying this parameter is found to produce a good agreement with the experimental results for each of the seven cases; the displaced volume is therefore the only parameter that is altered compared to the original simulations.

Reducing the displaced volume causes the load curves to spread further apart resulting in better alignment with both the magnitude and heat load sensitivity for all cases. This requires that the displaced volume of each scenario be altered differently. The changes made to the displaced volumes compared to the experimentally recorded values are shown in Table 4-3. The resulting simulations using these reduced displaced volumes are shown in Figure 4-13 through Figure 4-16. One area that remains different from the experimental results is the temperature span at high heat loads above the Curie point. This can specifically be seen in Figure 4-14 (right) and Figure 4-16 for the 40 W load case. Overall however, the majority of the curves are sufficiently aligned.

Table 4-3: Experimental and reduced displaced volumes necessary to align the experimental and simulated results.

Utilization	Frequency (Hz)	Experimental V_{disp} (mL)	Simulated V_{disp} (mL)
0.62	2	3.10	2.08
0.62	4	3.10	2.48
0.94	2	4.75	4.13
0.94	4	4.75	3.23
1.03	2	5.15	4.64
1.03	4	5.15	3.61
1.28	2	6.4	6.14

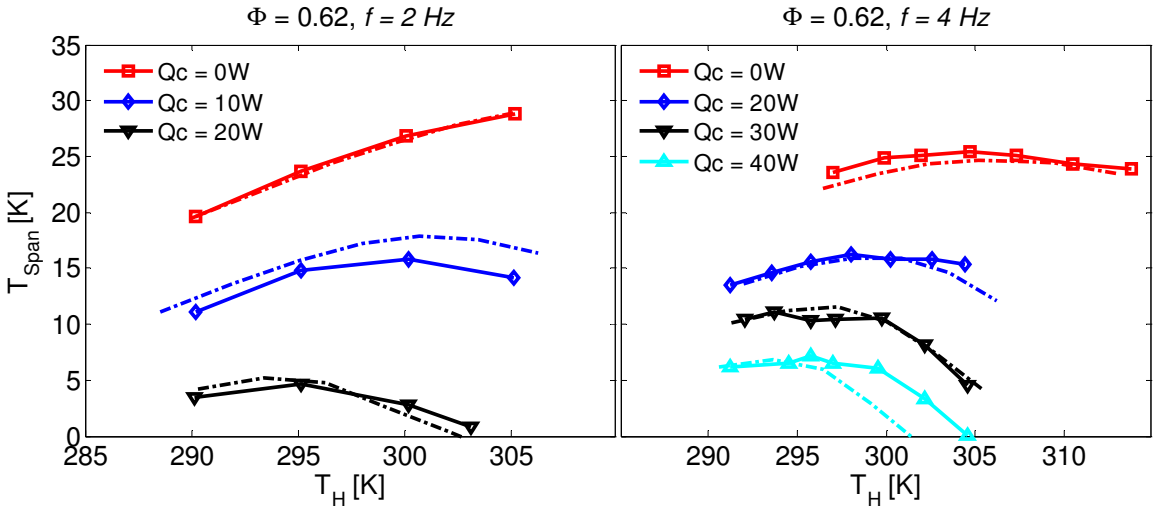

Figure 4-13: PMMR1 load curves using reduced utilizations at frequencies of 2 Hz (left) and 4 Hz (right) and Φ_{calc} = 0.62. Solid lines represent experimental data while dashed lines are simulated results.

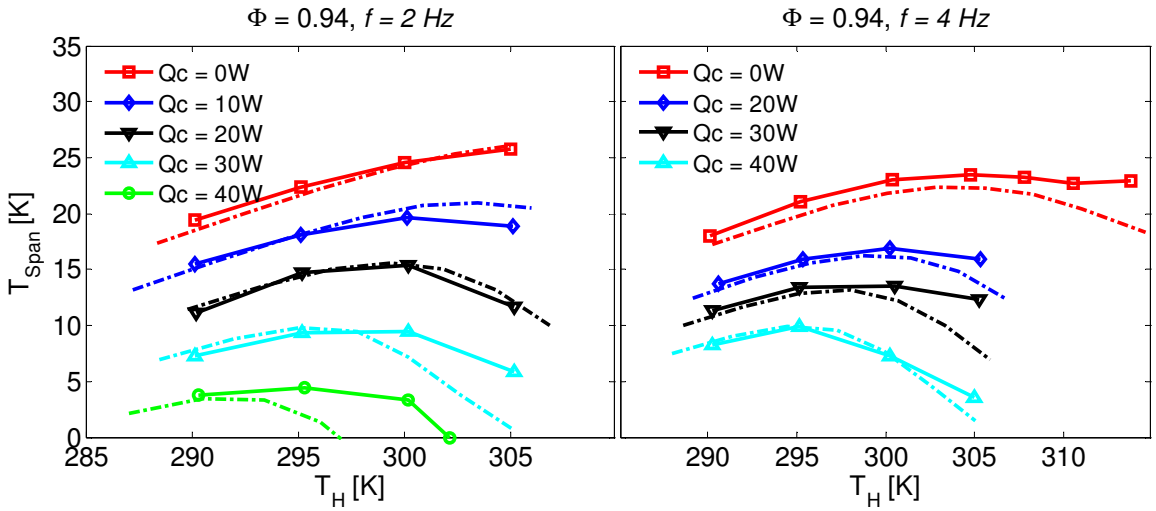

Figure 4-14: PMMR1 load curves using reduced utilizations at frequencies of 2 Hz (left) and 4 Hz (right) and Φ_{calc} = 0.94. Solid lines represent experimental data while dashed lines are simulated results.

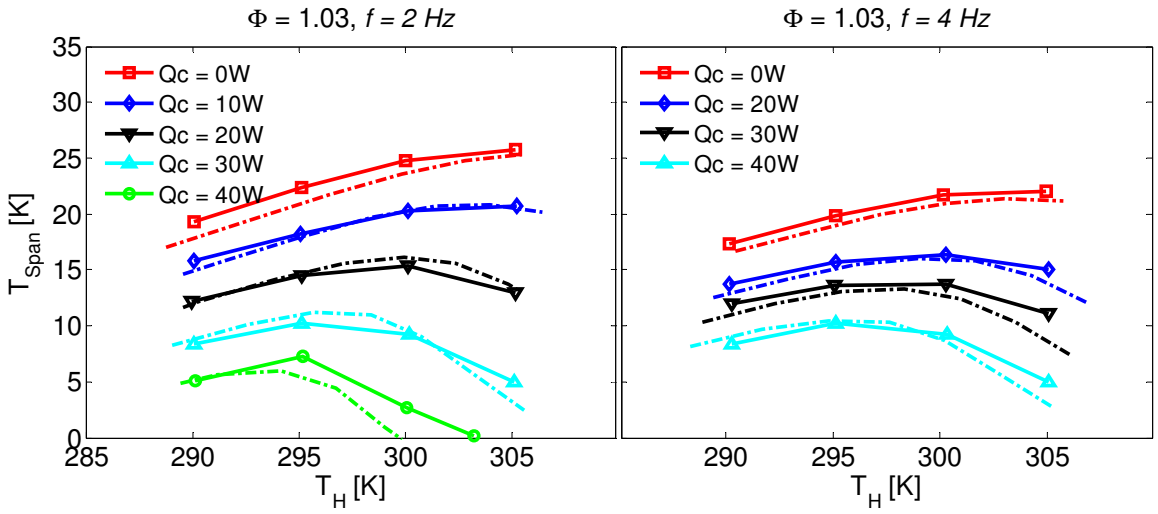

Figure 4-15: PMMR1 load curves using reduced utilizations at frequencies of 2 Hz (left) and 4 Hz (right) and Φ_{calc} = 1.03. Solid lines represent experimental data while dashed lines are simulated results.

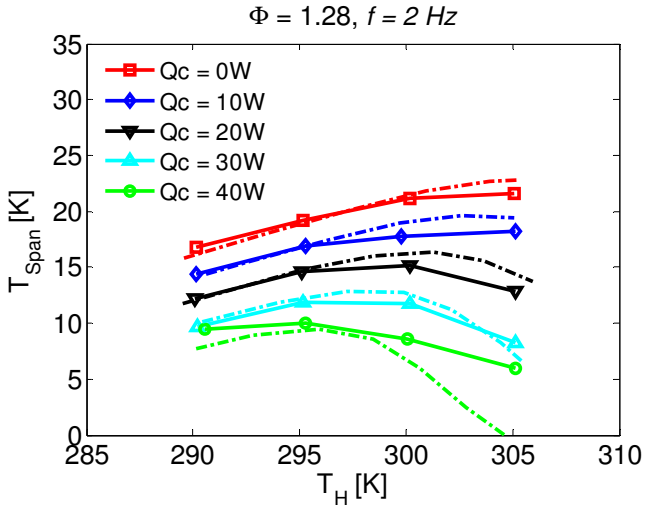

Figure 4-16: PMMR1 load curves using reduced utilizations at a frequency of 2 Hz and Φ_{calc} = 1.28. Solid lines represent experimental data while dashed lines are simulated results.

Reducing the displaced volume also has a direct influence on the system's utilization. The simulated utilizations in Figure 4-13 through Figure 4-16 are therefore different than the calculated utilizations. This difference is plotted in Figure 4-17.

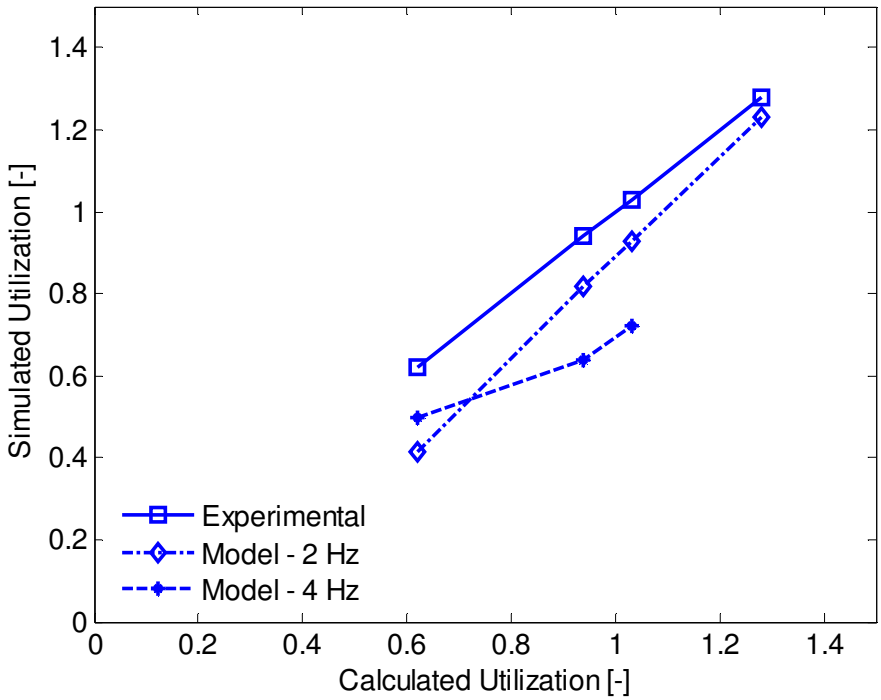

Figure 4-17: Experimental vs simulated utilizations required to match the experimental results to the model. Simulated utilizations are calculated using the reduced displaced volumes from Table 4-3.

From Figure 4-17 it can be seen that the 2 Hz tests required less reduction in utilization than the 4 Hz tests and form a linear set of points. Additionally, the higher utilizations required less of a reduction in order to match the experiments with exception of the lowest utilization. This is addressed further in Chapter 6.

This chapter was dedicated to the comparison of the simplified AMR model with experimental results from two different AMR devices, the AMRTA and the PMMR1. For the AMRTA device, the simulations produced good agreement with the experimental results for all of the tested scenarios which varied by heat load, utilization, material and regenerator length. The only modifications necessary are a decrease in the MCE of GdTb and an increase in the thermal conductivity in the temperature profile differential equation for the multilayer tests. For the PMMR1 results, the initial simulations provided only a partial agreement with the experimental data set. Reducing the displaced volume in the system, however, was found to improve the prediction substantially. The curves also had to be shifted by 4 K to align the peaks of the simulations with that of experiments. Implications of these modifications to the model are investigated in Chapter 6 of this thesis. The next chapter will focus on using the model in applications regarding multilayer regenerators. This includes varying the Curie temperature spacing and weighting between layers in a regenerator with more than one material.

Chapter 5 – Model Application

In the previous chapter, simulations from the simplified model are compared against experimental data from two different AMR devices. For a large variety of scenarios, simulated results agreed well with experimental data. In this chapter, the validated model is used as a predictive tool. One area of particular interest for improving AMR performance is the layering of materials within AMR's. Although it is known that layering a regenerator can improve the refrigerant capacity over single-layer AMR's [35], little research has been done with regards to material spacing and weighting of refrigerants in room temperature devices. For this reason, a two-layer regenerator is simulated and the effects of varying the Curie temperature spacing and weighting of materials are investigated. The concept of a maximum layering potential is then discussed.

5.1 Two-layer Simulations

It has been shown experimentally that strategically layering materials in room temperature devices increases the available temperature span of a regenerator [10]. Due to the time and cost of experiments, however, a means of predicting the Curie temperature spacing between layers as well as the weighting of the different materials that will give the best possible performance is needed. Simulations are subsequently performed for layered regenerators to provide further insight.

For these simulations it is assumed that all materials undergo second-order phase transitions with magnetocaloric properties similar to Gd, a representative second-order material. The MCE and Curie temperature of Gd is scaled and shifted to create material ordering at any chosen temperature (similar to how GdTb and GdEr are simulated in the previous chapter.) This removes the added constraint of obtaining a large amount of material data at different Curie temperatures and allows for a controlled comparison of the multiple factors affecting the performance of layered regenerators.

The first simulation replicates a two-layer regenerator using an equal amount of Gd and a simulated material whose Curie temperature is varied. This tests the effects of varying the Curie temperature spacing for second-order refrigerants. The next simulation

varies the proportion of each material in the regenerator. For simplicity, the same operating conditions as the two puck AMRTA experiments in Figure 4-3 are used. This includes a helium charge pressure of 9.5 atm, frequency of 0.65 Hz and an equivalent particle diameter of 560 μm. In addition, the predictive scenarios assume no-load conditions. The implications of this are discussed in the following chapter.

5.1.1 Varying Curie Temperature Spacing

As shown in Figure 4-3, when Gd is layered with either GdTb or GdEr, the regenerator outperforms the Gd-Gd regenerator by as much as 50 %. This is because each half of the regenerator operates closer to its peak MCE rather than one type of material having to operate over the whole temperature range. To gain a better sense of the effects of the Curie temperature spacing between materials, a two-layer regenerator is simulated. One half of the regenerator is Gd while the other half is a material with the same MCE as Gd but a different Curie temperature. The Curie temperatures of the simulated materials are listed in Table 5-1 while their respective MCE curves are shown in Figure 5-1.

Table 5-1: Curie temperatures of the simulated materials.

Simulated Material	**T_{Curie} (K)**
A	289
B	279
C	269
D	259
E	249

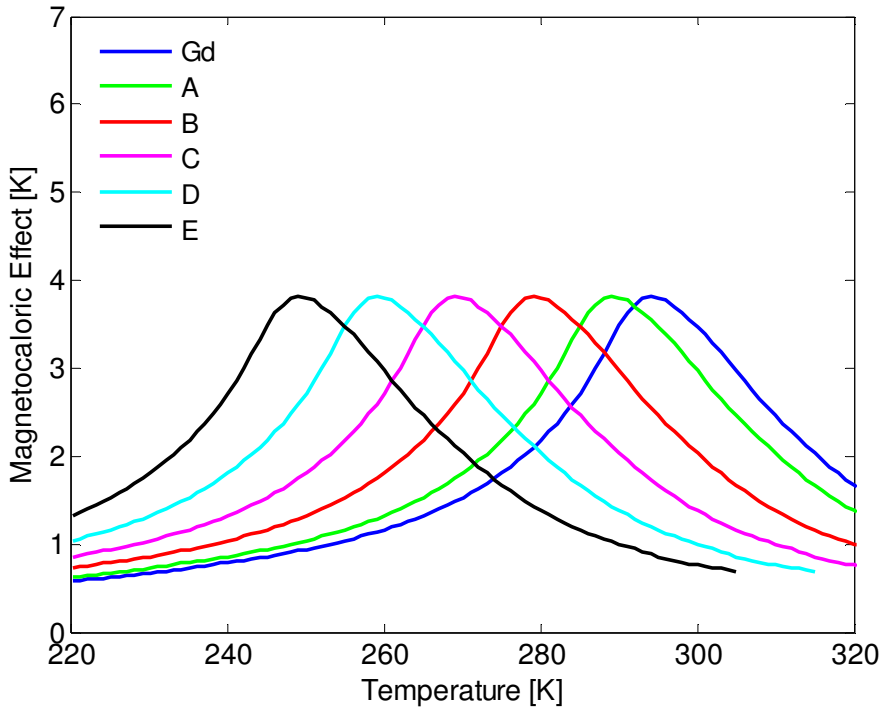

Figure 5-1: MCE of Gd and the simulated materials used in the multilayer simulations. As seen in the figure the MCE of the simulated materials are the same as Gd but T_{Curie} has been shifted.

Using these materials, the multilayer simulations for various T_{Curie} spacing are seen in Figure 5-2. The maximum temperature span occurs at T_H = 305 K when the simulated material has a Curie temperature of 269 K (material C.) As the T_{Curie} spacing is increased further, the temperature span becomes relatively constant over a broad range of hot end temperatures. It is important to note that while the maximum temperature span occurs when the simulated material has a Curie temperature of 269 K, the optimum operating condition depends on what the desired hot end temperature, T_H, of the device would be. For instance, at T_H = 290 K, the highest temperature span is achieved with a Curie temperature of 259 K. Additionally using a T_{Curie} within 5 K of 269 K does not change the result to a large degree, which gives a little more flexibility in design. This optimal Curie temperature would change if a heat load were applied to the system.

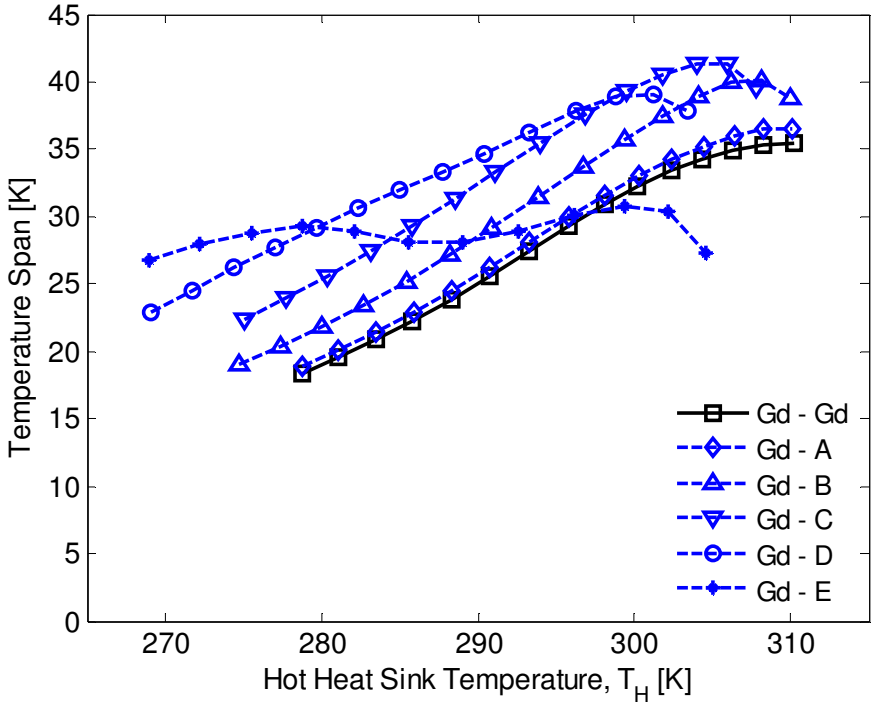

Figure 5-2: Generalized two-layer regenerator with varying Curie temperature under no load. The top layer is Gd while the cold end layer has a specified T_{Curie}. The MCE of both layers is equal to Gd.

5.1.2 Varying Material Weighting

In the previous section, the weighting of materials in the regenerator is fixed while the Curie temperature of the simulated material is allowed to vary. In this section, T_{Curie} of the cold end layer is fixed at 269 K while the material weighting is varied. This provides further knowledge about the effect of weighting materials when the layers have different properties.

Figure 5-3 shows the predicted temperature spans for a two-layer regenerator where the proportion of Gd is varied. Three curves are plotted in this figure. The top curve represents the maximum temperature span of the regenerator at the specified Gd proportion for all boundary conditions that equate to a zero applied cooling power. The bottom two curves show the temperatures spans for fixed T_H values of 300 K and 290 K. The results from this plot imply that if one wants to maximize temperature span only, a 0.5 proportion of Gd is best. If a hot end temperature of 300 K or 290 K is desired however, then the optimum Gd proportion shifts down to 0.4 and 0.2, respectively.

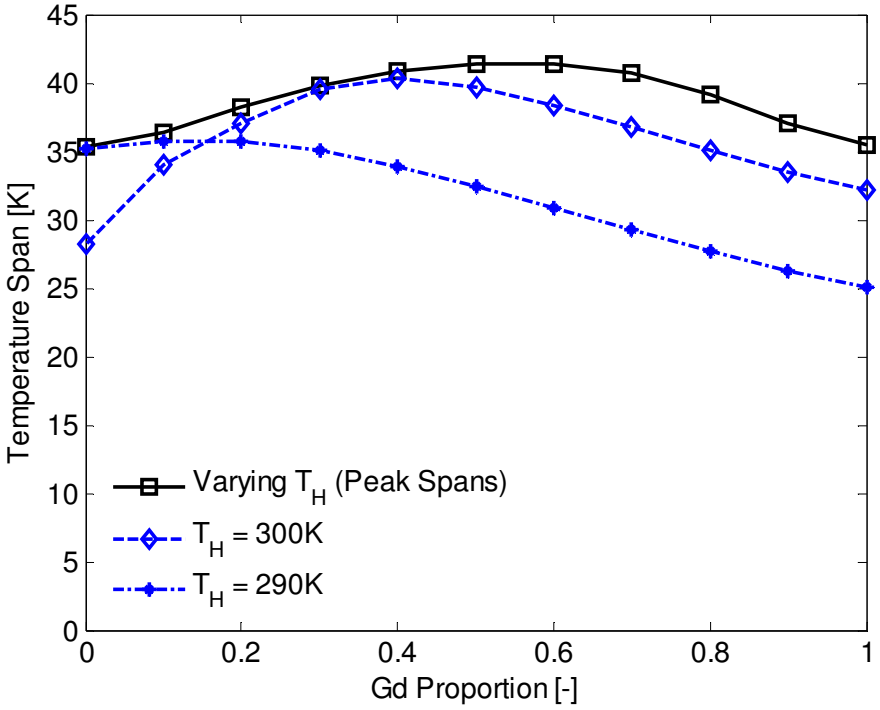

Figure 5-3: The proportion of Gd in a two-layer regenerator is varied. T_{Curie} of the cold end material is fixed at 269 K. The plot shows peak temperature span of each proportion of Gd as well as the temperature spans at fixed T_H values.

The impact of Gd weighting can be also repeated using a reduced MCE for the cold end material. This is more likely to be seen in actual experiments where the material properties of the two layers differ. A reduction of 25 % in the simulated material's MCE is chosen and the resulting curves are plotted in Figure 5-4. In the peak temperature span curve, this shifts the optimum Gd proportion up to approximately 0.7 from 0.5. Likewise for T_H values of 300 K and 290 K the optimal Gd proportion increases to 0.5 and 0.3, respectively.

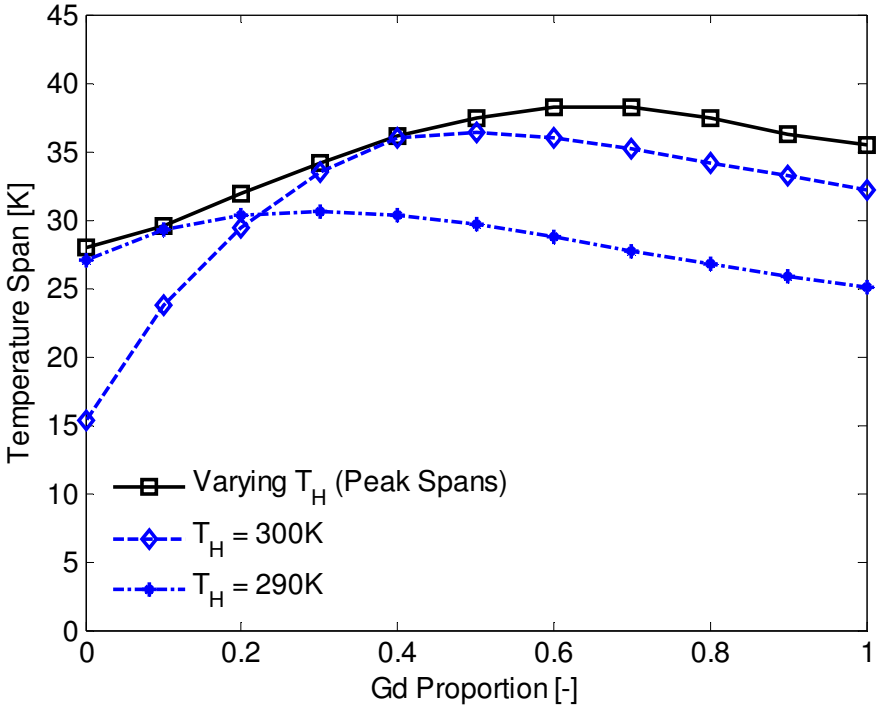

Figure 5-4: The proportion of Gd in a two-layer regenerator is varied. T_{Curie} of the cold end material is fixed at 269 K while the MCE is 75 % that of Gd. The plot shows peak temperature span of each proportion of Gd as well as the temperature spans at fixed T_H values.

A similar analysis to the one in Figure 5-3 was also performed by Dikeos using a more detailed numerical model [34]. Instead of using a simulated material on the cold end layer, however, he used a two-layer regenerator of Gd and $Gd_{0.85}Er_{0.15}$ where the proportion of Gd was again varied. A comparison between the simplified model presented in this thesis and results from Dikeos' model is shown in Figure 5-5. Although the magnitude of the temperature spans between the two models differs, the sensitivity of the temperature span to the proportion of Gd is similar. In this simulation the hot heat sink temperature is set to 290 K.

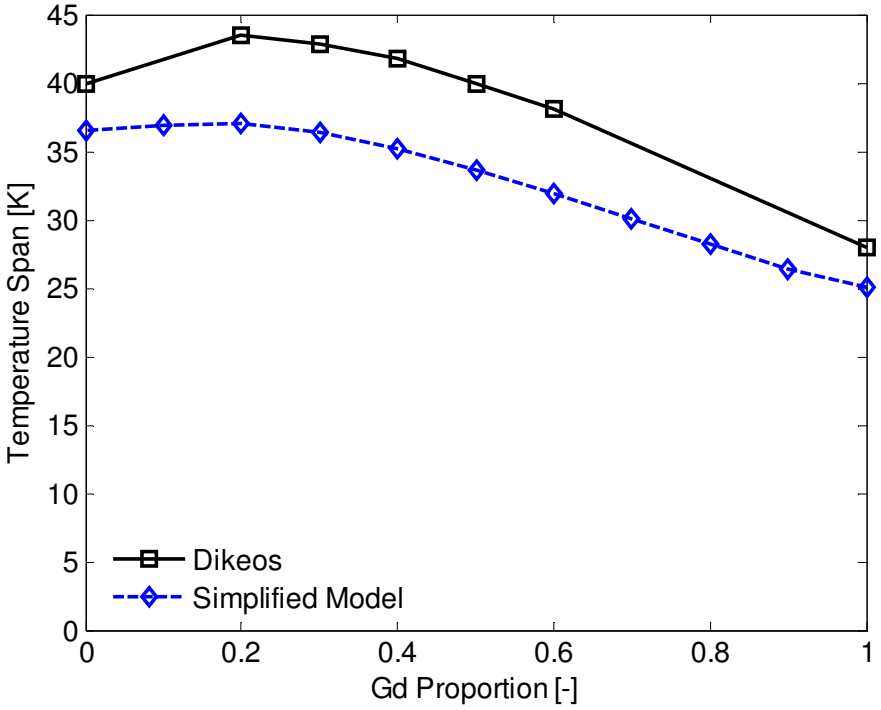

Figure 5-5: The proportion of Gd in a two-layer Gd-GdEr regenerator is varied. The results are plotted using a fixed T_H = 290 K.

The effects on the temperature span of varying the Curie temperature spacing and material weighting in two-layer regenerators has been documented for a single set of operating conditions. All of these scenarios used the same device setup so that only the relative performance of varying the material properties was investigated. The next section discusses the impact of device design on increasing performance through layering.

5.2 Maximum Layering Potential

In an AMR device a large variety of conditions contribute to the achievable temperature span across the regenerator. This section investigates the impacts that a device, and primarily the magnetic field profile, has on the potential of layering to increase performance over single-layer regenerators. To quantify this effect, the concept of a maximum layering potential is introduced.

The maximum layering potential is defined here as the temperature span achievable if a material were to operate at its peak MCE across the entire temperature span of the

regenerator (i.e. ideal layering). This essentially assumes that one would have an infinite number of identical materials, but a slightly different Curie temperature, and then layer them together in a perfect combination. Determining the potential of ideal layering is important as it can provide an upper limit for the performance of a given material, device or operating condition.

Numerically, the maximum layering potential can be simulated by implementing the following conditions into the model:

$$MCE(T) = MCE_{max} \tag{35}$$

$$C_p(T) = C_p(T_{Curie}) \tag{36}$$

To demonstrate the effect of the above assumptions, the maximum temperature spans for three scenarios are compared to no-load, single-layer equivalents. These single-layer scenarios are summarized in Table 5-2. The first scenario replicates the operating conditions of the two-puck AMRTA experiments while the second scenario replicates the PMMR1 with a utilization of 1.03 and frequency of 2 Hz. The final scenario is identical to the second but assumes the magnetic profile of the PMMR1 device resembles a sine wave as opposed to the sine squared wave described in Section 4.2.1, Figure 4-8. A demagnetization of 29 % is used in both cases.

Table 5-2: Summary of single-layer regenerator operating conditions

Device	Material	Frequency (Hz)	Utilization	Peak Fields (T)	Simulated Field (T)
AMRTA	90g of Gd	0.65	0.15	0 – 2	0.30 – 1.71
PMMR1	55.3g of Gd	2	1.03	0.1 – 1.45	0.66 – 1.15
PMMR1 modified field	55.3g of Gd	2	1.03	0.1 – 1.45	0.30 – 0.97

For the PMMR1 operating conditions, a comparison of the magnetic waveforms over a cycle is shown in Figure 5-6 while the resulting MCE's used in the simulations are in Figure 5-7. As can be seen, the MCE of the modified waveform has a substantially larger peak than the current device. Additionally, the slope of the MCE curve is larger. This implies that operating further from the Curie point results in a greater absolute drop in the

MCE for the modified PMMR1 device than for the actual PMMR1 device. As will be shown, this has a large impact on the ability of using layering to increase the temperature span of a device.

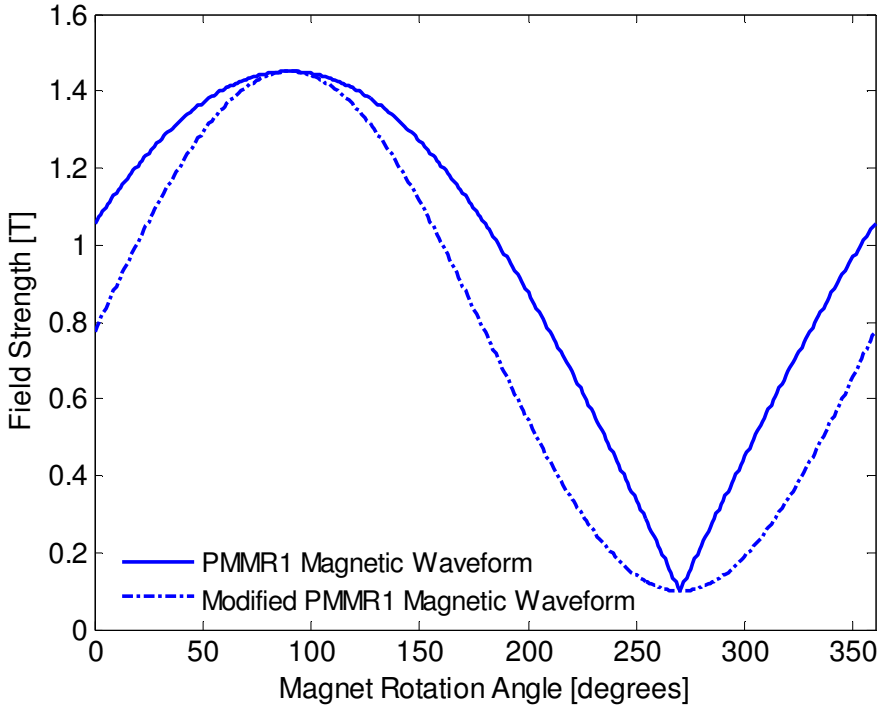

Figure 5-6: Comparison of the magnetic waveform for the PMMR1 and modified PMMR1 device.

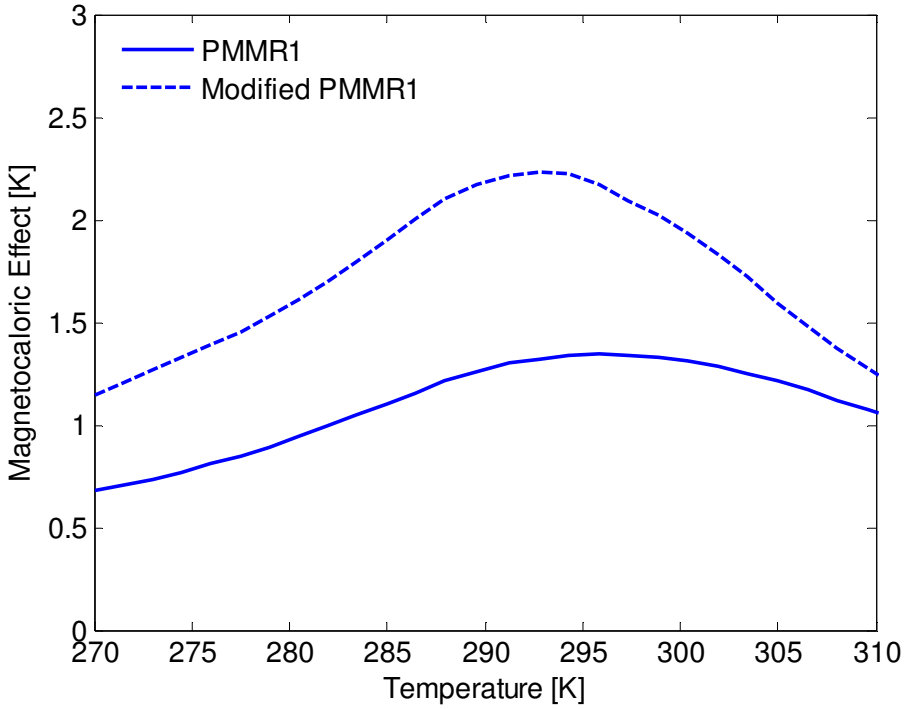

Figure 5-7: Comparison of the MCE for the PMMR1 and modified PMMR1 device.

The scenarios in Table 5-2 can now be simulated. For each scenario the no-load temperature span is plotted using a single-layer of Gd. The same three scenarios are also plotted with the conditions stated in Eqns (35) and (36). Figure 5-8 shows the achievable temperature span using ideal layering with the same operating conditions as the single-layer cases. The maximum layering curves for the PMMR1 devices are sloped due to heat leaks from the environment as previously described in Eqn (34).

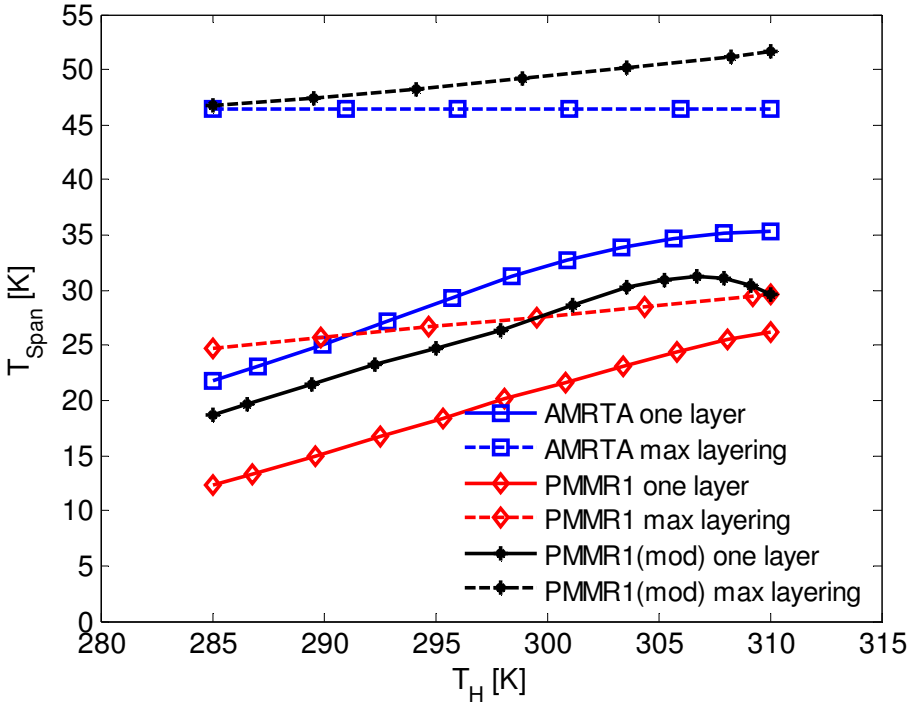

Figure 5-8: Maximum layering potential using peak MCE Gd properties for three scenarios for a single set of operating parameters.

From the above figure, the modified waveform for the PMMR1 device provides a much larger layering potential than the current setup although the single-layer performances of the two setups are comparable. The results for the AMRTA device setup are also similar to the modified PMMR1 waveform although the operating conditions between the two setups are quite different. Further discussion about the maximum layering potential is provided in the next chapter.

The model has been used to investigate several of the parameters which influence the performance of multilayer regenerators. This included the Curie temperature spacing and weighting of a two-layer regenerator. For a Gd-GdEr regenerator the model was also compared to a more detailed model with comparable results. Finally, the influence of a device on the layered regenerators was investigated. This indicated the importance of magnetic field profiles on layering potential. The next chapter will provide further insight on the results from this chapter and Chapter 4. In particular, the assumptions used in the validation procedure will be identified.

Chapter 6 – Discussion

This chapter is dedicated to a more detailed analysis of the results obtained in Chapters 4 and 5. This includes analysis of the AMRTA and PMMR1 validation results as well as the performance of layered regenerators.

6.1 VALIDATIONS

6.1.1 ACTIVE MAGNETIC REGENERATOR TEST APPARATUS

In all of the tested scenarios the model results follow the trends of the experimental results. For the single-layer tests, the simulated Gd, GdEr and GdTb regenerators show good agreement with both the magnitude and sensitivity of the temperature span curve. In the case of the GdTb regenerator this required a reduction in the MCE. A similar problem for this material was observed with a more detailed numerical model [34]. In that case, a better fit was obtained by increasing the static conductivity of the bed. The fact that both assumptions are effective in correcting model predictions is supported by the simplified study in [22] where a non-dimensional parameter determining the cooling power and efficiency of an AMR was found:

$$I \equiv \frac{\Phi}{\kappa}\frac{\Delta T}{T} \tag{37}$$

In [34], the impact of increasing the static conductivity decreases I; likewise, in this work, decreasing the adiabatic temperature change leads to a decrease in I. In effect, the adjustments produce the same result in the governing energy balance. Both approaches may be justified given the lack of detailed measurements for the particular batch of material being used, and due to the irregular particle shapes and resulting uncertainty in regenerator thermal effectiveness. This reduced MCE for GdTb is also used in the multilayer simulations.

Generally, the multilayer regenerator simulations are in good agreement with experimental results. One exception is the Gd-GdEr and Gd-GdTb-GdEr regenerators at temperatures high above the Curie point of Gd. At these points the temperature span decreases rapidly with temperature and follows the same path for both regenerators. This discrepancy may represent a difficulty in the model to solve the temperature profile

differential equation (Eqn (13)) when one of the materials in the regenerator is almost inactive, in this case the GdEr layer. This expresses one of the benefits that a time dependent model has over the simplified model as the development of the temperature span over time can be analyzed instead of only the steady state solution. Moreover, in order for the multilayer regenerators to be solved, an increase in the non-dimensional thermal conductivity in Eqn (13) by a factor 3 is also required. This is due to the difficulty of solving AMR's at low utilizations where the thermal mass of the working fluid is substantially less than the regenerator matrix. For the multilayer regenerators tested the utilization is ~0.15 for the two puck experiments and ~0.1 for three pucks, which is very low. No conductivity modifications are required for the single-layer tests where the utilization is ~0.3. Practical cryogenic applications would likely require utilizations in the range of 0.2 to 0.3 [36] while the utilizations of room temperature devices, which use liquid working fluids, are typically greater than 0.6 [33].

The next AMRTA validation compares the heat load variation with temperature span at a fixed regenerator hot end temperature. Analysis of the model results allows for a breakdown of the individual losses to be quantified. At the observed T_H value of 292 K, the primary system loss is due to the effectiveness of the regenerator to transfer energy from one end to the other. Although an unavoidable loss, this stresses the need for continued research in passive regenerator optimization projects. Performing the same heat load analysis at T_H = 305 K shows that the viscous dissipation losses become much more prevalent when operating above the Curie temperature. In the case of varying utilization and the heat load at various temperatures some differences are seen between the experiments and the model. These discrepancies are expected due to the simplicity of the model relative to the physics occurring in the experiments.

Examples of this are seen in the physical representation of the AMR including the characteristic particle diameter and simulated RMS field strength. The model also assumes that pure Gd, GdTb and GdEr exist in the regenerator. In the experiments, however, the regenerator materials are coated in a thin layer of epoxy which increases interfacial heat transfer resistance, acts as a parasitic thermal mass, and may cause flow-channeling. Additionally, since the cooling power of the AMRTA experiments are small (~20W), any errors in modeling the losses can have a large impact on the expected

temperature span as compared to experiments with large cooling capacities. Some errors also exist in the replication of GdEr and GdTb specific heat curves from Gd data as the specific heat curves of second-order materials are similar but not exactly the same.

Overall, in the operating space defined by the AMRTA, the model is found to produce continuous curves based upon the results in Figure 4-2 through Figure 4-6. In general, T_H values below the Curie point solve faster than those above the Curie point. The model also has difficulty solving for the temperature distribution at T_H values high above the Curie point when both large pressure drops and low utilizations (<0.15) are present. This is due to the non-dimensional thermal conductivity becoming too low relative to the pressure drop to solve the energy balance differential equation. It is found that setting a minimum value on the conductivity in the differential equation rectifies this problem. Subsequent testing of the pressure drop used in the model found that for gaseous working fluids pressure drop plays an important role in the degradation of the temperature span at temperatures above the Curie point. It was noted by Tura [10] that obtaining data with T_H values high above the Curie points is in general experimentally unstable and difficult to replicate, particularly for varying heat load scenarios at low utilizations.

6.1.2 Permanent Magnet Regenerative Refrigerator

Simulations for the PMMR1 device are able to replicate the experimental curves with sufficient accuracy. Unlike the AMRTA device, however, the PMMR1 setup requires a larger number of assumptions to be made in order to do so. This primarily includes the numerical representation of the magnetic waveform and the effective displaced volume through the regenerator.

Before simulations could be run, representative high and low RMS fields needed to be extracted from the experimental waveform of the PMMR1 device. In this analysis, an average peak field dependent on the regenerator length is simulated (reference Figure 4-7.) In an actual experiment, however, the ends of the regenerator would feel a reduced magnetic field compared to the centre of the regenerator. For a 55 mm regenerator this difference between the centre and the end is 0.12 T [33] which could have an important impact on the performance. For little computational cost, a spatially varying field could be implemented into the model to account for this effect. This would make use of the

multipoint boundary conditions described in Section 3.2. This analysis, however, is outside of the current scope of the thesis. For completeness, a similar analysis should also be performed for the minimum magnetic field which varies to a much lesser degree. Another area where approximation is necessary is the demagnetization effects in the PMMR1 device. Modeling results found demagnetization effects to reduce the magnetic field by 24 % for a 55 mm regenerator while using a value of 29 % aligns better with the curvature of the experimental results. Taking into account the required RMS approximation and the averaging of the peak field strength, however, a deviation of 5 % from the modeled demagnetization seems reasonable in order to fit the experimental data.

The next assumption required to fit the data pertains to the displaced fluid through the system. With no modifications to the displaced volume, the simulations compare relatively well with the 2 Hz experiments but are very different for the 4 Hz cases. Reducing the displaced volume is found to sufficiently correct the data for the higher frequency tests while providing improvements to the 2 Hz predictions. Plotting the reduced utilizations against the calculated utilizations subsequently provides a useful plot (Figure 4-17.) This plot shows that the 4 Hz cases, with the exception of the lowest utilization, require more of a reduction than the 2 Hz cases. Additionally, the 2 Hz data is linear and near a utilization of 1.28, thus almost no reduction is required. Based upon these observations, frequencies close to 1 Hz and higher utilizations should require no adjustments to be simulated with reasonable accuracy.

The cause of this effect is unidentified at the moment, however, and requires further investigation. Because of the similar errors in magnitude for the 0.8 Hz simulation in the AMRTA device, it may be an issue when operating at higher frequencies. This may indicate physics not captured in the simplified model that occur in experimental devices at these high frequencies.

The last required modification for the agreement between the PMMR1 results is a shift in the Curie temperature of the material by 4 K. This shift is most likely due to both a difference in the material properties as compared to material data and a result of the simulated field strength. In an actual device, the magnetic field goes from 0.1 T to 1.45 T while the RMS approximation used in simulations is from 0.66 T to 1.15 T. While this

field approximation may be valid from a magnitude point of view, approximating at these fields results in the peak MCE effectively being shifted to a higher temperature than the actual field strength. A representation of this is shown in Figure 6-1 where the peak MCE is shifted by approximately 4 K due to the lower field approximation.

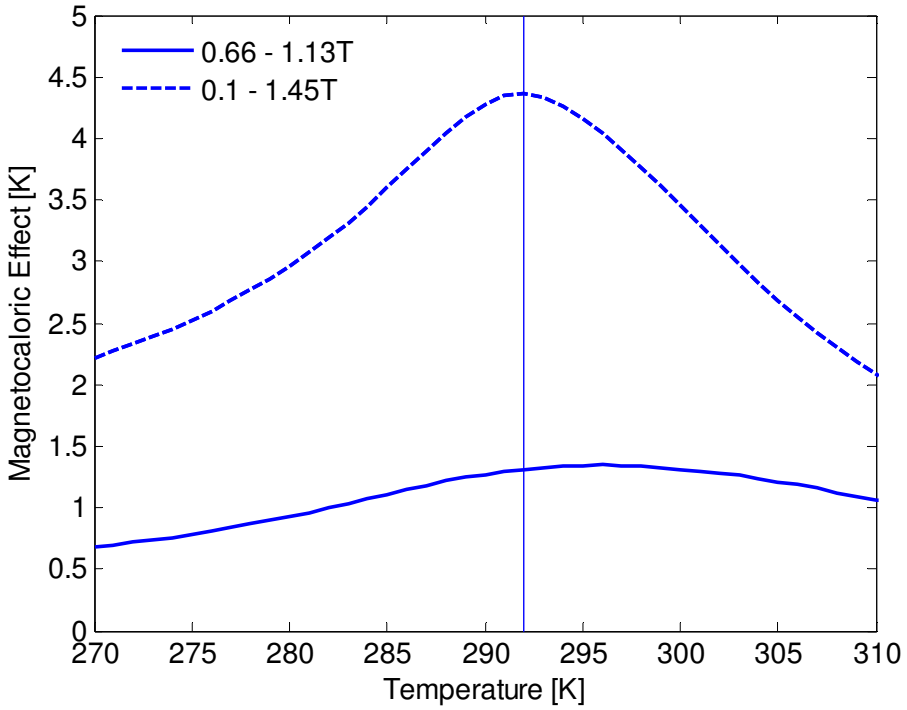

Figure 6-1: Movement in the peak MCE for a field variation from 0.1 T to 1.45 T and a variation from 0.66 T to 1.13 T.

At the higher utilizations of the PMMR1 device, operation of the model is more consistent than the AMRTA simulations. All data points take an almost equivalent amount of time to solve regardless of whether they are above or below the Curie point. Additionally, the relatively large thermal mass ratio caused by using a liquid working fluid means that no modifications are required to the thermal conductivity in order to solve low utilizations or multilayer regenerators.

Overall, the simulated results predicted both the AMRTA and PMMR1 experiments sufficiently accurate enough to provide a basis for proceeding with the model in optimization and design cases where general trends of the performance are of primary

importance. Using similar methods to those proposed in Chapter 4, the model can also be adapted to other devices for further validation or predictive purposes.

6.2 Model Applications

6.2.1 Two-layer Tests

To better understand the effects that material properties have on layering, several two-layer regenerators are simulated. The hot end layer of the regenerator is chosen as Gd while the cold end layer is simulated to have the same MCE as Gd but is shifted or scaled as needed.

The first data set in Chapter 5 tests the effects of changing the Curie temperature spacing between the two layers. Initially, as the Curie spacing is increased, the maximum no-load temperature span also increases. A maximum span is reached at a low end Curie temperature of 269 K. However, one additional consideration with layering regenerators is that the optimum Curie temperature spacing also depends upon the single-layer performance. In this case the Gd-Gd regenerator is able to reach a peak span of approximately 35 K at T_H = 305 K. This means that the cold end temperature, T_C, would be 270 K, right in the operating region of the 269 K cold layer material. If the Gd-Gd peak no-load span had been 15 K, however, then it is likely that a low end Curie temperature closer to 280 K would give the highest peak span. This is because a material with T_{Curie} = 269 K is not fully utilized in that case.

This same logic can be applied to scenarios where a heat load is applied. As a heat load is applied to a system the temperature span of the regenerator ultimately decreases. This means that the optimal Curie temperature spacing between the materials also depends on the applied heat load. For the same two-layer regenerator setup (where Gd is paired with a material of the same MCE but different Curie temperature), Figure 6-2 shows the optimal cold end Curie temperature for a varying heat load. It should be noted that these presented Curie temperatures gave the largest peak temperature span; however, using a Curie temperature within 5 K in either direction gives very similar results. This is due to the relatively broad MCE curve for Gd and second-order refrigerants in general. As the heat load approaches its maximum value the optimal Curie temperature approaches that of Gd.

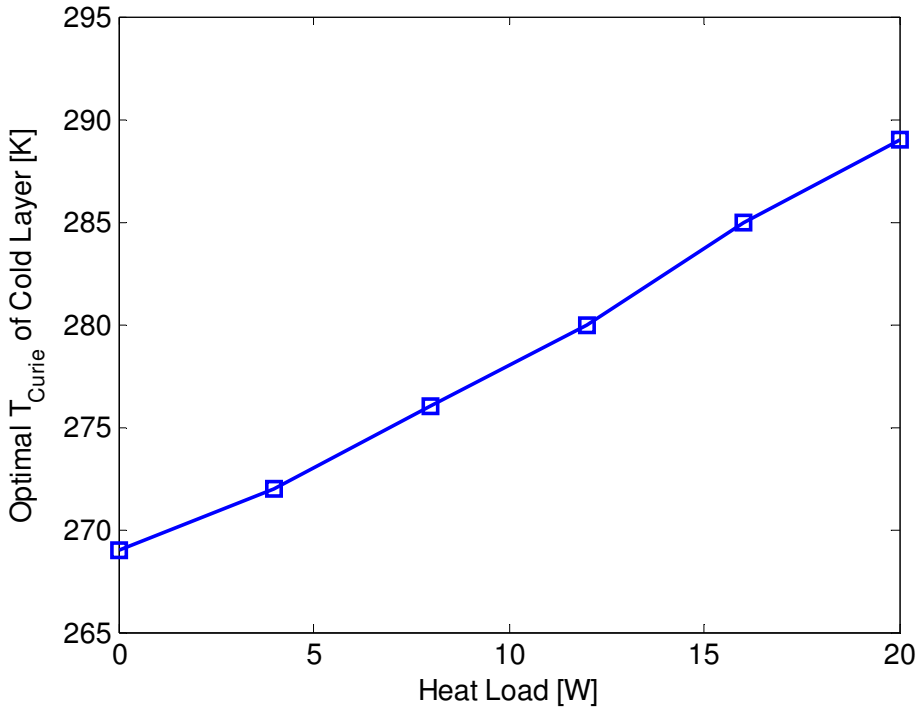

Figure 6-2: The effect that heat load has on the optimal Curie temperature spacing for a two-layer regenerator.

The second set of two-layer tests focuses on the weighting of each material in the regenerator. In this case, T_{Curie} of the simulated layer is fixed at 269 K. It is found that when both regenerators have the same MCE, the Gd proportion that gives the peak temperature span is an even 0.5. This is due to the relative symmetry of the MCE curve for second-order materials about the Curie point. For materials with an asymmetric MCE curve, the impact of layer weighting is expected to be more significant. Furthermore, if a specific T_H value is desired, the Gd proportion will shift either higher or lower than the even layer weighting.

For the scenario where the MCE of the lower end temperature is reduced, weighting shifts more to the Gd side as one would expect. Had the cold end material had a larger MCE than Gd, the opposite effect is expected. Finally, although the weighting simulations are done with only a single simulated Curie temperature of 269 K, the weighting results are fairly indicative of other Curie spacing's as well.

6.2.2 Maximum Layering Potential

While the previous results focus on varying material properties under fixed operating conditions, this investigation fixes the material properties and addresses the impact that devices have on layering. The concept of a maximum layering potential is introduced and is defined as the maximum temperature span available if the regenerator operates at its peak MCE across the entire temperature domain. The representative material chosen for the simulations is again Gd. The temperature spans of three different scenarios are then plotted using the properties of Gd and then using only the peak MCE of Gd.

The AMRTA scenario, shown again in Figure 6-3, reaffirms the results by Tura [10] which concluded that layering a regenerator can increase the maximum temperature span. Also plotted in the figure is the best two-layer regenerator from Section 5.1.1 which uses the same operating conditions. While the top line represents the maximum layering potential, the best two-layer scenario represents a significant improvement over the one layer Gd test. The same analysis can be done for more than two layers with incrementally smaller improvements toward the maximum temperature span.

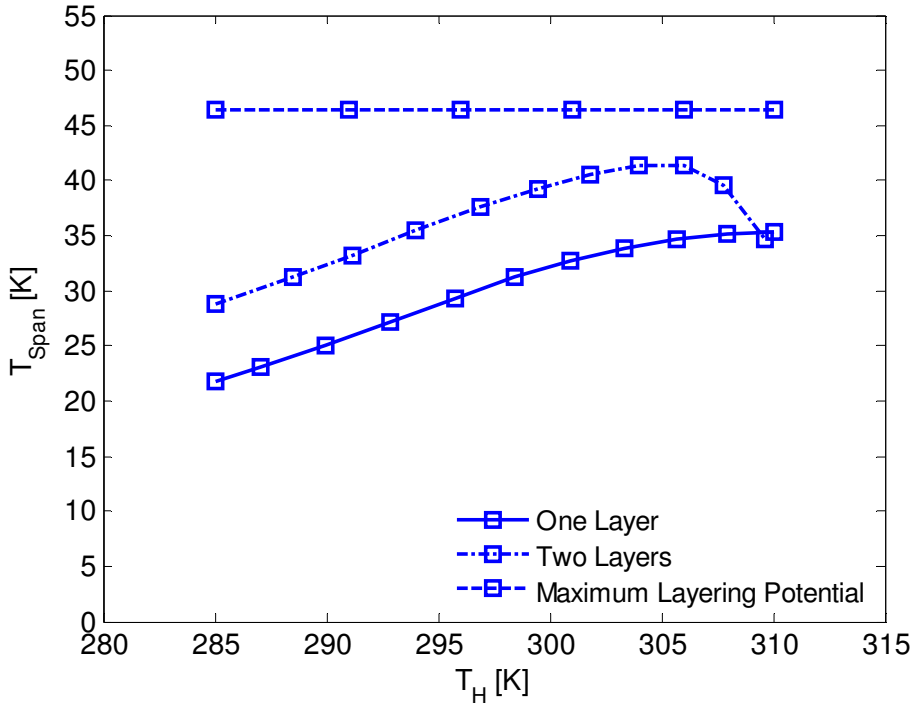

Figure 6-3: Using the properties of Gd, the no-load temperature span is plotted assuming one, two and infinite layers. The two-layer test is made of Gd and simulated material, C, where the simulated material has the same MCE as Gd but a Curie temperature of 269 K.

For the maximum layering potential of the PMMR1 scenarios the results can give important information about the impact of device design on layering potential. One case is the PMMR1 setup described in the validation section. The other case is identical to the PMMR1 setup with the exception of using a magnetic waveform in the form of a sine wave. As shown in Figure 5-7, this modified waveform greatly increases the peak MCE. These single and infinite layer results are plotted again in Figure 6-4. As can be seen, the single-layer Gd tests are only about 5 K apart despite the increase in MCE for the modified waveform. The ability for the temperature span of the regenerator to be improved, however, is far superior for the modified PMMR1 case. This is because the steeper MCE curve with the modified setup allows for much more improvement than the flat MCE curve as one operates away from the Curie point.

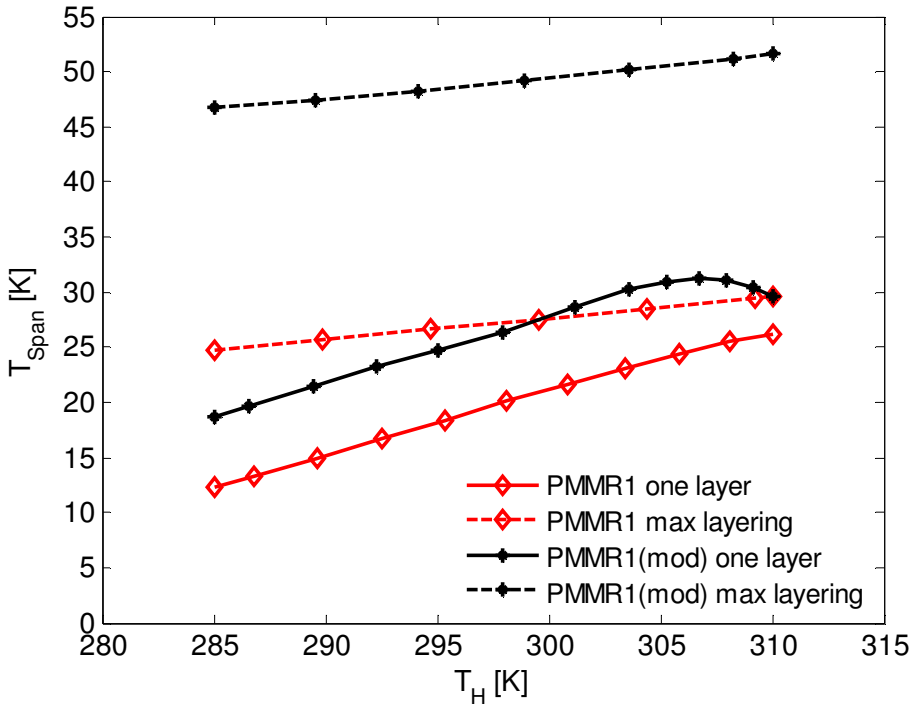

Figure 6-4: Using the properties of Gd the no-load temperature span is plotted assuming one and infinite layers for the PMMR1 and PMMR1 (modified) scenarios.

As shown in these predictive results, the performance of a layered regenerator is impacted by a large number of factors. This emphasizes the need for quick modeling

solutions in guiding the layering choices for experiments that would ultimately save experimental time and finances.

This chapter provided a closer analysis of the AMRTA and PMMR1 validations as well as the multilayer predictive results. Areas, where assumptions or modifications are required, have been identified and provide future direction for improvements. The next section will make conclusions as to the model's ability to be used as a predictive tool for studying AMR devices.

Chapter 7 – Conclusions

This thesis has discussed the development and testing of a simplified model for predicting the performance of AMR devices. The objective was to create a model capable of being used as a tool in parallel with experimental results. The model can then be used as confirmation for results, guide future experiments, predict regions currently unobtainable to an apparatus and assist in the improvement and design of new devices. Additional objectives for the model required it to have a low computational cost, be simplistic in its operation and be easily adaptable to future devices.

In an attempt to meet these objectives, the theory and assumptions governing the model were created with both numerical simplicity and an accurate representation of the AMR physics in mind. This led to a steady state, one-dimensional approximation for the active magnetic regenerator that can be solved at a very low computational cost. Accounting for individual system losses and converting the convective heat leak into an equivalent thermal conductivity also allowed the model to provide accurate predictions for the magnitude and trends of experimental results. This was tested through validation with two different experimental devices, the AMRTA and the PMMR1, whose experimental data varied over a large operating range. Once validated, the model was also used for studying multilayered regenerators using materials simulated from Gd. From the combination of these results it is concluded that the simplified model can be used as a research tool for both gaseous and liquid AMR systems.

A great deal of effort was also taken in the implementation of the simplified model into the computational domain. The objective was to make the model accessible to all members of an AMR research group regardless of their level of experience in modeling, heat transfer or thermodynamics. A particular example of this is the internal function which automatically adjusts the boundary conditions to produce T_H vs T_{Span} curves for user specified, applied loads. Furthermore, since the model produces a steady state solution, whose spatial mesh size is taken into account internally in MATLAB, the inputs into the model pertain only to the operating conditions of the AMR and not modeling parameters such as the time step. The ability also exists for other materials and devices to be added to the model's database with relative ease.

The primary benefit of this AMR model compared to other works is the high level of correlation achieved with the experimental results for the given simplicity of the model. This allows for a large number of simulations to be run in a short amount of time while still trusting the accuracy of the outputs. This was possible due to the large breadth of experimental results available for validation and realistic modeling of the device specific losses. The model however is not without its flaws. As seen during validations several modifications were required to align the data sets. While some of these modifications are justifiable, others require further investigation. Additionally, the regenerators tested in this analysis were relatively small irregular particles and spheres, meaning that internal temperature gradients are minimal. This would not be the case for larger particles or parallel plate regenerators and may be an area where the detail of higher-order models is needed.

7.1 RECOMMENDATIONS

Based upon the presented results several areas of further research can be recommended for the simplified model. The first is to adapt the model for use in optimization and costing programs. Because of the model's ability to provide quick solutions, the large parameter space of AMR devices can be swept for optimal operating conditions. A mapping of the device efficiency and cooling power for different parameters can then be made to aid in the AMR design process. Additionally, physical parameters such as the regenerator length can be linked to the length of the magnet. The device performance at a given field strength can then be linked with the magnet cost necessary to produce the field. This type of design would balance the importance of performance and cost requirements on future AMR devices.

Recommendations also exist to improve the overall model and its representation of complex AMR devices. One particular example is a better representation of the magnetic field profile of the PMMR1 device. This can be done by implementing a simplified demagnetization function into the model. Additionally, the model can be adapted to allow for a spatially varying high and low magnetic field instead of the averaging over the length of the bed which is currently done. This can be done using the same multipoint boundary conditions currently used for simulating multilayer regenerators.

Furthermore, the simplified model should be tested against a higher-order model to determine the impacts that the derivation assumptions have on performance. It may then be possible to provide correction factors to the simplified model that improve future predictions without altering the computational cost.

As a final recommendation, simulations for the model should continually be compared to new experimental results with varying operating parameters. This includes different regenerator and fluid flow configurations. It would also be a good idea to test the simplified model against lower frequency PMMR1 results to see if a reduction in the displaced volume is still necessary to match experimental results.

REFERENCES

[1] Steyert WA. Magnetic refrigeration for use at room temperature and below. J. de Physique Collogue 1978;39;1598

[2] Warburg E, Ann. Phys., 1881;13;141

[3] Weiss P, Piccard A. Sur un nouveau phénomène magnétocalorique. Compt. Rend. Ac. Sci. 1918;166;352

[4] P. Debye, Einige Bemerkungen zur Magnetisierung bei tiefer Temperatur. Ann. Phys. 1926;81;1154–1160

[5] W.F. Giauque, A thermodynamic treatment of certain magnetic effects. A proposed method of producing temperatures considerably below 18 absolute. J. Am. Chem. Soc. 1927;49;1864–1870

[6] Brown GV. Magnetic heat pumping near room temperature. J. Appl. Phys. 1976;47;3673

[7] Barclay JA, Steyert Jr. WA. Active Magnetic Regenerator. United States Patent 4332135, 1982

[8] Rowe A. Thermodynamics of active magnetic regenerators: Part I. Cryogenics, 2011:52:111-118

[9] Richard MA, Rowe, A, Chahine R, Bose T, Barclay JA. "Towards Magnetic Liquefaction of Hydrogen: Experiments with an Active Magnetic Regenerator Test Apparatus." Canadian Hydrogen and Fuel Cell Conference, Vancouver, 2003

[10] Tura A. Active Magnetic Regenerator Experimental Optimization. MASc Thesis, University of Victoria, Victoria 2005

[11] Engelbrecht K. A Numerical Model of an Active Magnetic Regenerator Refrigerator with Experimental Validation. PhD Thesis, University of Wisconsin-Madison, 2008

[12] Legait I, Kedous-Lebouc A, Rondot L. Numerical simulation and analysis of the refrigerant bed behavior using fluent software. In: Egolf, P.W. (Ed.), Third International Conference on Magnetic Refrigeration at Room Temperature. 2009

[13] Risser M, Vasile C, Engel T, Keith B, Muller C. Numerical simulation of magnetocaloric system behavior for an industrial application. Int. J. Refrigeration 2010:33(5):973-981.

[14] Nielsen KK, Bahl CRH, Smith A, Pryds N, Hattel J. A comprehensive parameter study of an active magnetic regenerator using a 2D numerical model. Int. J. Refrigeration 2010;33:753–64.

[15] Tusek J, Sarlah A, Zupan S, Prebil I, Kitanovski A, Poredos A. A numerical optimization of a packed bed AMR. In: Egolf, P.W. (Ed.), Fourth International Conference on Magnetic Refrigeration at Room Temperature. International Institute of Refrigeration. 2010

[16] Liu M, Yu B. Numerical investigations on internal temperature distribution and refrigeration performance of reciprocating active magnetic regenerator of room temperature magnetic refrigeration. Int. J. Refrigeration 2011:34:617-627

[17] Dikeos J, Rowe AM, Tura A. Numerical analysis of an active magnetic regenerator (AMR) refrigeration cycle. Adv. Cry. Eng., 2006;823;993-1000

[18] Nielsen KK, Tusek J, Engelbrecht K, Schopfer S, Kitanovski A, Bahl CRH, Smith A, Pryds N, Poredos A. Review on numerical modeling of active magnetic regenerators for room temperature applications. Int. J. Refrigeration 2011:34:603-616.

[19] Zhang L. Sherif SA, Veziroglu TN, Sheffield JW. Second law analysis of active magnetic regenerative hydrogen liquefier. Cryogenics 1993;33;667-674

[20] Zhang L, Sherif SA, DeGregori AJ, Zimm CB, Veziroglu TN. Design and optimization of a 0.1 ton/day active magnetic regenerative hydrogen liquefier. Cryogenics 2000;40;269-278

[21] Rowe A, Barclay J. Ideal magnetocaloric effect for active magnetic regenerators. J. Appl. Phys 2003;93;1672-1676

[22] Rowe A. Thermodynamics of active magnetic regenerators: Part II. Cryogenics, 2011:52:119-128

[23] Ergun S. Fluid flow through packed column. Chemical Engineering Progress, 1952:48:125-127

[24] Kaviany M. Principles of Heat Transfer in Porous Media, Springer, New York, NY 1995

[25] Nam K. Jeong S. Measurement of cryogenic regenerator characteristics under oscillating flow and pulsating pressure. Cryogenics, 2003:43:575–581.

[26] Vortmeyer D., Schaefer RJ. Equivalence of one- and two-phase models in packed beds: one dimensional theory. Chemical Engineering Science 1974;29;485-491

[27] Wakao N. Kaguei S. Heat and Mass Transfer in Packed Beds. Gordon and Breach Science Publishers, New York, NY, 1982

[28] Engelbrecht K. The effect of internal temperature gradients on regenerator matrix performance. Transactions of the ASME, 2006;128;1060-1069

[29] Kittel P. Eddy current heating in magnetic refrigerators. Advances in Cryogenic Engineering 35B, edited by R.W. Fast, Plenum, 1990;35B;1141-1148

[30] Tura A, Roszmann J, Dikeos J, Rowe A. Cryogenic Active Magnetic Regenerator Test Apparatus. Adv. Cryo. Eng., 2006;823;985-992

[31] Callen, H. Thermodynamics. John Wiley and Sons, New York, 1960

[32] Zimm CB, Ludeman EM, Severson MC, Henning TA. Materials for Regenerative Magnetic Cooling Spanning 20K to 80K. Adv. Cryo. Eng., 1992:37:883-890

[33] Tura A, Rowe A. Permanent magnet magnetic refrigerator design and experimental characterization. Int. J. Refrigeration 2011:34:628-639

[34] Dikeos J. Development and Validation of an Active Magnetic Regenerator Refrigerator Cycle Simulation. MASc Thesis, University of Victoria, Victoria 2006

[35] Tsukagoshi T, Matsumoto T, Hashimoto T, Kuriyami T, Nakagome H. Optimum structure of multilayer regenerator with magnetic materials. Cryogenics, 1997:37:11-14

[36] Zimm CB, Johnson JW, Murphy RW. Test results on a 50K magnetic refrigerator. Advances in Cryogenic Engineering 41B, edited by R.W. Fast, Plenum, 1995;41B;1675-1681